A widespread and ancient bacterial machinery assembles OmcS cytochrome nanowires essential for extracellular electron transfer

Graphical Abstract

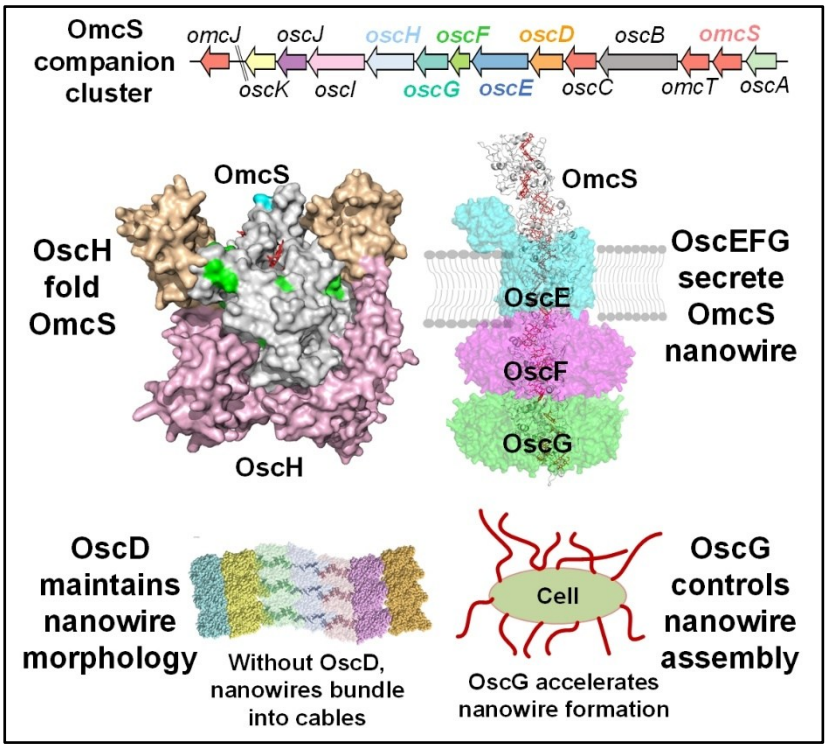

Authors

Cong Shen, Aldo I. Salazar-Morales, Wonhyeuk Jung, Joey Erwin, Yangqi Gu, Anthony Coelho, Kallol Gupta, Sibel Ebru Yalcin, Fadel A. Samatey and Nikhil S. Malvankar

Correspondence

nikhil.malvankar@yale.edu (N.S.M.),
cong.shen@yale.edu (C.S.)

In brief

In phylogenetically diverse environmentally-important bacteria, an ancient, evolutionary-conserved modular biosynthetic gene cluster assembles cytochrome OmcS into electrically conductive nanowires. Modulating the production of key cluster proteins accelerates bacterial respiration via extracellular electron transfer by stimulating nanowire production and bundling nanowires. These demonstrated design principles could enable control of microbial growth.

Keywords: extracellular electron transfer, microbial nanowires, *Geobacter*, cytochrome, secretion systems, electronic conductivity, biogeochemical cycling, prolyl isomerase, DEAD-box, biosynthetic gene cluster

Highlights

- **An *omcS*-companion (*osc*) cluster in diverse bacteria assembles cytochrome nanowires**
- **OscH, OscEFG & OscD ensure folding, secretion & morphology of nanowire respectively**
- **Overexpression of ATP-bound OscG accelerates cell growth by overproducing nanowire**
- **Heme loading splits OscD and Δ*oscD* accelerates cell growth with bundling nanowires**

A widespread and ancient bacterial machinery assembles OmcS cytochrome nanowires essential for extracellular electron transfer

Cong Shen[1,2,3*], Aldo I. Salazar-Morales[1,2], Wonhyeuk Jung[4,5], Joey Erwin[1,2,] Yangqi Gu[1,6,7], Anthony Coelho[1,2], Kallol Gupta[4,5], Sibel Ebru Yalcin[1,2], Fadel A. Samatey[1,2] and Nikhil S. Malvankar[1,2,8*]

[1]Microbial Sciences Institute, Departments of [2]Molecular Biophysics & Biochemistry, [3]Microbial Pathogenesis, [4]Cell Biology, [6]Molecular, Cellular & Developmental Biology, [5]Nanobiology Institute, Yale University. West Haven, Connecticut, USA, 06516. .[7]Present address: MRC Laboratory of Molecular Biology, University of Cambridge, UK. .[8]Lead Contact. *Correspondence: nikhil.malvankar@yale.edu (N.S.M.), cong.shen@yale.edu (C.S.)

Microbial extracellular electron transfer (EET) drives various globally-important environmental phenomena and has biotechnology applications. Diverse prokaryotes have been proposed to perform EET via surface-displayed "nanowires" composed of multi-heme cytochromes. However, the mechanism that enables only a few cytochromes to polymerize into nanowires is unclear. Here, we identify a highly-conserved *omcS*-companion (*osc*) cluster that drives the formation of OmcS cytochrome nanowires in *Geobacter sulfurreducens*. Through a combination of genetic, biochemical, and biophysical methods, we establish that prolyl isomerase-containing chaperon OscH, channel-like OscEFG, and β-propeller-like OscD are involved in the folding, secretion, and morphology maintenance of OmcS nanowires, respectively. OscH and OscG can interact with OmcS. Furthermore, overexpression of *oscG* accelerates EET by overproducing nanowires in an ATP-dependent manner. Heme loading splits OscD and Δ*oscD* accelerates cell growth with bundling nanowires. Our findings establish the mechanism and prevalence of a specialized and modular assembly system for nanowires across phylogenetically-diverse species and environments.

Microbial respiration via EET drives various globally important environmental processes[1], including biogeochemical cycles of metals[1] and greenhouse gases[2,3], and has applications for bioelectronic sensing of environmental contaminants[4] and controls pathogen growth[5,6]. Well-known pathways of EET[1] use soluble molecules[5] and membrane-bound monomeric cytochromes[7], which limits microbial performance due to their limited range, especially under natural flow conditions. In contrast, *Geobacter* species perform long-range (>1 μm) EET by directly contacting extracellular electron acceptors via conductive appendages called "nanowires", thus eliminating the need for diffusive redox mediators.

This remarkable ability to produce nanowires positions the *Geobacteraceae* family as a predominant presence in anoxic sediments and soil environments where energy availability is limited[8]. The *Geobacteraceae* family is pivotal in efficiently bioremediating toxic organic and metal contaminants in groundwater[9], and is prevalent in co-cultures with methanogens[10,11], where they actively engage in direct interspecies electron transfer (DIET), a particular case of EET to syntrophic microbes. Additionally, they are frequently enriched in bioelectrochemical systems, which convert organic waste into electricity[12]. Electrode-grown *G. sulfurreducens* biofilms show high conductivity to confer the highest current densities among isolated electroactive microbes[13], facilitated by forming nanowire networks that aid electron transport across distances exceeding hundreds of micrometers[14,15]. Thus, *Geobacter* species are among the most efficient organisms for EET, making them highly valuable for biotechnological applications in electrocatalysis, corrosion, and the production of fuels.

Structural and localization studies have shown that microbial nanowires - conductive filaments on the cell surface during EET are polymerized cytochromes made up of OmcS[16-18] and OmcZ[19-21], whereas pili show low conductivity and remain intracellular during EET[22]. Moreover, OmcS-mutated cells produce OmcE cytochrome filaments under non-EET growth conditions[23]. However, a continuing assumption of pili as nanowires[24], and the fact that many cytochromes involved in EET cannot form filaments[7] have led to controversy about the nanowire identity and function[16,25-27].

Cryo-electron microscopy (cryo-EM) of OmcS nanowires shows a seamless stacking of hemes[17,18], which enables highly efficient electron transport over micrometer distances[28,29]. These findings of high electronic conductivity in OmcS nanowires are significant because out of 111 cytochromes in *G. sulfurreducens*, OmcS is the first nanowire-forming cytochrome discovered as essential for DIET[30,31] and EET to Fe(III) oxides abundant in subsurface[32]. Indeed, cytochromes, which are abundant in the subsurface during uranium bioremediation, function similarly to OmcS[33]. The *omcS* operon, comprising *omcS* and *omcT*, is also important for EET to electrodes during the initial stages of biofilm growth[34] measured over the first several days[35,36]. The OmcS nanowires also show ultrafast excited-state (<100 fs) heme-to-heme electron transfer that increases nanowire photoconductivity by 100-fold[28]. This photoconductivity could account for biocatalytic ability of living biofilms[37,38].

While these studies highlight the importance of OmcS nanowires in EET, the molecular mechanisms of their assembly and functions are required beyond the structural determination[23]. The challenge for identifying nanowires beyond *G. sulfurreducens* is that not all cytochromes with closely stacked hemes can be polymerized, and the assembly mechanism of cytochromes into nanowires is not known. For example, another model electroactive bacteria *Shewanella oneidensis* also performs EET via multi-heme cytochromes that are not known to polymerize[7]. The lack of knowledge about the assembly mechanism impedes the broad application of OmcS nanowires. Previous attempts failed to exhibit OmcS nanowires by heterologously expressing *omcS* gene alone[39,40], except a single study reported the reconstituted OmcS filaments from *S. oneidensis*[41] without confirming the filament identity[42]. Therefore, here we focused on determining the mechanism of OmcS nanowire assembly.

Results and Discussion

Identification of the *osc* cluster. Using comparative genomes[43], we found high evolutionary conservation of OmcS homologs among *Geobacter* species. Remarkably, a cluster next to *omcS* is also conserved, which we named the *osc* (*omcS*-companion) cluster (**Fig. 1A, Table. S1**). In addition to *Geobacteraceae* family, both OmcS and the *osc* cluster are conserved among diverse environmentally important bacteria, including EET-performing species across multiple phyla, such as Thermodesulfobacteriota, Myxococcota, and Aquificota phyla (**Fig. 1A & S1A, Table. S2 & S3**). For example, Candidatus *Desulfofervidus auxilii* (HotSeep-1) is a DIET-performing syntrophic partner of methane-oxidizing archaea[2], whereas many other species can perform EET[44,45].

Complementary DNA (cDNA) analysis showed that most of the *osc* cluster (*oscB-K*) in *G. sulfurreducens* can form an intact operon (**Fig. S2A**) separate from the *omcST* operon[32]. Further analysis showed that the intergenic region of *oscE-F* expressed much lower than other intergenic regions, which suggests a possible gap in the transcription of *oscB-K* (**Fig. S2A**). During the transition from exponential to stationary phase, the expression of the *osc* cluster is coregulated with *omcS* expression (**Fig. 1B & S2B-D**). The *oscE-I* showed the highest expression increase (**Fig. 1B & S2B-D**). Only *oscD* showed decreased expression, suggesting its distinct role from other *osc* genes. Therefore, we hypothesized that the *osc* cluster could be involved in forming OmcS nanowires.

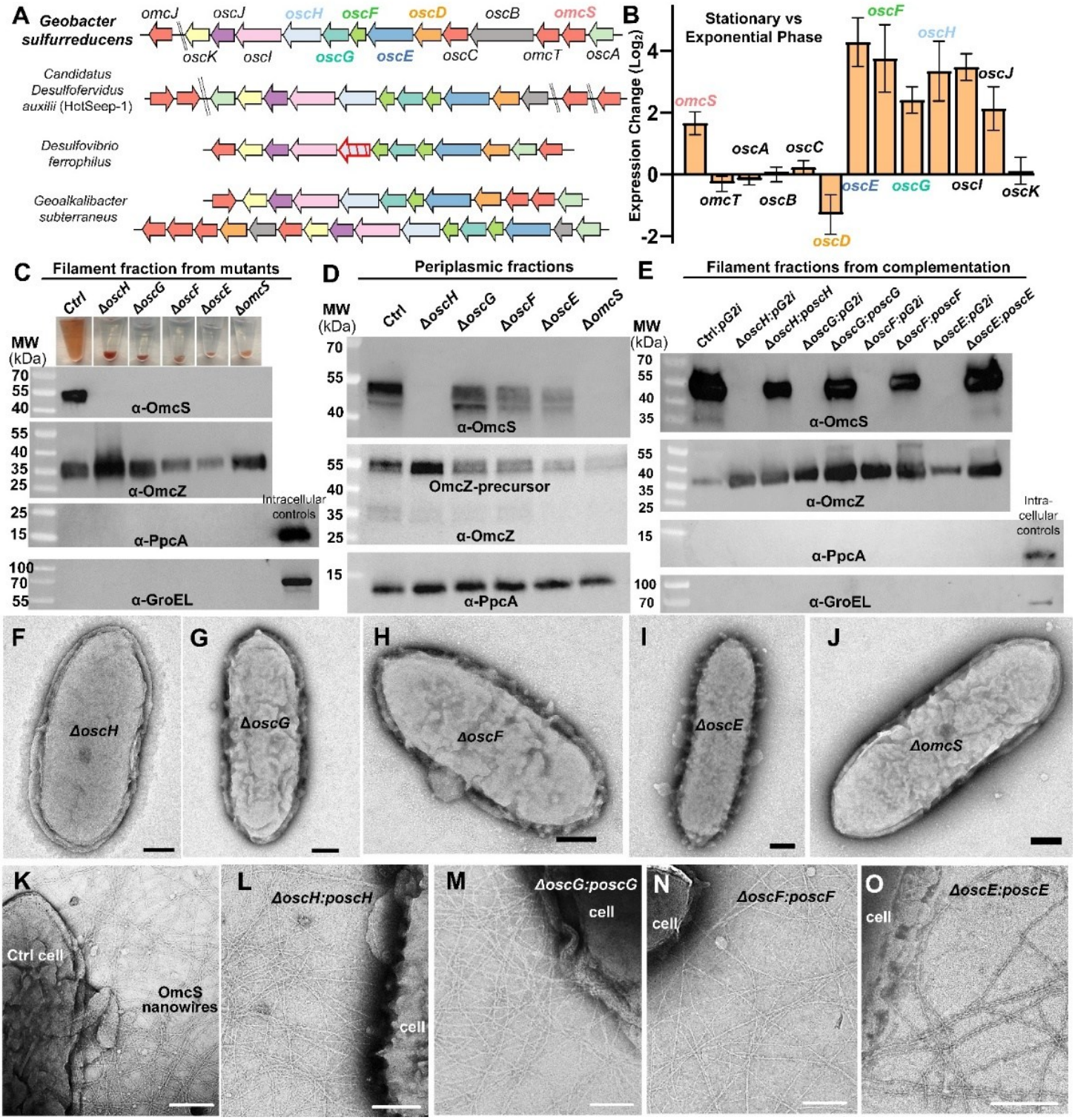

Fig. 1 The widespread *osc* cluster encodes OscEFGH which are essential for the formation of OmcS nanowires. A, Genomic organization of the *osc* clusters with homologs share the same color. Non-conserved genes are in grey. Partial *oscH* is striped in red for *D. ferrophilus* that lacks OmcS nanowires. **B,** Relative expression change in the *osc* cluster as *G. sulfurreducens* wild type (WT) assembles OmcS nanowires by transitioning from exponential (**Fig. S2C**) to stationary phase (**Fig. S2D**), using the housekeeping gene *rpoD* as reference. Error bars, SEM (n=4 biological replicates). Δ*omcS* and Δ*oscE-H* cells cannot assemble and secrete OmcS nanowires, as shown by **C,** sample appearance and immunoblots of filament fractions, **D,** immunoblots of periplasmic fractions and **F-K**, TEM images. Nanowire defect is rescued in complemented cells as shown by **E,** immunoblots and **L-O,** TEM images. *pG2i* : empty plasmid. All scale bars, 200 nm except **N**, 100 nm.

The *osc* cluster is required to form OmcS nanowires. We disrupted the *osc* cluster by inserting a plasmid (denoted as pK18) into *oscD* upstream of *oscE-K*, using *G. sulfurreducens* strain CL-1[46] as a control strain (hereafter, *Ctrl*). We have routinely used the *Ctrl* strain to obtain purified OmcS nanowires in liquid cultures. Mass spectrometry confirmed that OmcS was the most prominent cytochrome in the filament fraction, whereas other known filament-forming cytochromes, such as OmcE, were at very low abundance (**Table. S4**). In *G. sulfurreducens*, though OmcS paralogs (OmcT, OscC and OmcJ) share more than 50% protein sequence identity with OmcS. Still, only OmcS showed the highest expression (**Fig. S2D**) and protein abundance in filament fraction (**Table S4**). This expression pattern may explain the lack of nanowire formation by other OmcS paralogs in this study.

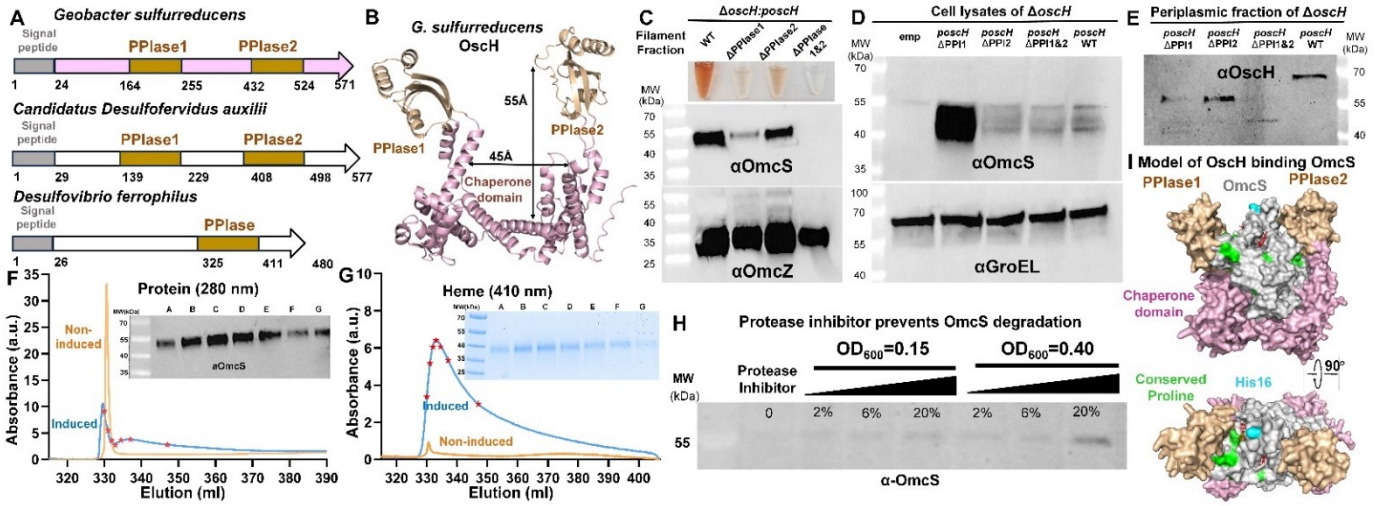

Fig. 2 OscH helps fold intracellular OmcS. **A,** Schematic of *oscH* domains. **B,** AlphaFold model of OscH from *G. sulfurreducens*. pLDDT > 90 for most residues. Immunoblots of OmcS in **C,** filament fraction**, D,** cell lysates, and **E,** of OscH in periplasmic fraction from mutants related to OscH prolyl isomerase domains. GroEL: loading control. Affinity purification of Strep-tagged OscH from *G. sulfurreducens* yielding chromatograms of **F,** protein (absorbance at 280 nm) and **G,** heme (at 410 nm), with gels as insets, that indicates OmcS interacts OscH *in vivo*. Red stars: sampling positions A-G in gels. **H,** Increasing the protease inhibitor concentration (%) prevents OmcS from degradation in early- and mid-exponential Δ*oscH* cells. **I,** Docking of OscH model holding OmcS (PDB: 6ef8) showing conserved prolines (green) and Histidine 16 (cyan).

This *oscD-K* disruption inhibited the formation of OmcS nanowires (**Fig. S3A**). In contrast, disruption of regions unrelated to the *osc* cluster did not inhibit the formation of OmcS nanowires (**Fig. S3A**). Furthermore, OmcZ nanowires could still assemble, suggesting that the *osc* cluster is specifically required to assemble OmcS nanowires (**Fig. S3A**). Gene annotations suggested that OscD is a β-propeller protein, OscH contains peptidyl-prolyl isomerase domains for protein folding, OscE is a β-barrel protein typically located in the outer membrane, and both OscF and OscG are lipoproteins (**Table. S1**). Consistent with their putative roles in nanowire secretion and assembly, the expression of individual *oscDEFGH* genes significantly changed when cells assembled nanowires (**Fig. 1B**). Due to this OmcS nanowire-associated expression change and similarity to known bacterial secretion systems, we focused on evaluating the role of *oscDEFGH* in nanowire assembly and secretion.

In-frame deletions of *oscE, oscF, oscG, oscH* and *omcS* inhibited the assembly of OmcS but not OmcZ nanowires in liquid cultures, as revealed by Coomassie and heme staining (**Fig. S3B**), immunoblotting of filament fractions (**Fig. 1C**) and negative staining transmission electron microscopy (TEM) (**Fig. 1F-K**), confirming *oscEFGH* involved in the formation of OmcS nanowires. The periplasmic (PpcA) and cytoplasmic (GroEL) controls confirmed the lack of cellular contamination in filament fractions (**Fig. 1C**). The defect in nanowire assembly was also visible to the naked eye as filament fractions of mutants precipitated as pellets. In contrast, nanowires from *Ctrl* cells showed a homogeneous red solution (**Fig. 1C**).

OmcS remained in the periplasm of Δ*oscE,* Δ*oscF* and Δ*oscG* mutants, indicating the involvement of OscEFG in the secretion of OmcS nanowires (**Fig. 1D**). The lower and upper bands observed in the immunoblots of periplasmic OmcS (**Fig. 1D**), following extended gel electrophoresis, are likely indicative of two OmcS forms corresponding to the states before and after heme incorporation, as the molecular weight difference of ~4 kDa corresponds to six hemes in OmcS. Periplasmic fractions also contained the OmcZ nanowire precursor (~50kDa) (**Fig. 1D**) in contrast to nanowire-forming OmcZ (~30kDa) in filament fractions[19] (**Fig. 1C**), indicating that the periplasmic and filament fractions did not contaminate each other. The decrease of OmcZ nanowires in some mutants (**Fig. 1C & Fig. S3**) could be due to the removal of *osc* proteins such as OscE, predicted to be a β-barrel outer membrane protein. Deletion of the putative porin may trigger the envelope stress response[47] to affect the secretion of OmcZ nanowires. The OmcS nanowire assembly in the *osc* mutants was restored by expressing the deleted genes on an inducible plasmid, and not when empty vector pRK2-Geo2i (pG2i) was present, as shown by immunoblots (**Fig. 1E**), Coomassie and heme staining (**Fig. S3C**), and TEM images of complemented cells displaying OmcS nanowires on their surface (**Fig. 1L-O**). This successful complementation of *osc*-related genes confirmed that the defect in nanowire assembly is not due to any pleiotropic effect.

OscH helps the folding of intracellular OmcS and inhibits degradation. OmcS is absent in both filament and intracellular fractions of Δ*oscH* cells (**Fig. 1C, 1D, 2D & 2H**). The lack of OmcS in Δ*oscH* was not due to a transcriptional defect because Δ*oscH* expressed higher *omcS* than the *Ctrl* strain (**Fig. S4A**). To understand the role of OscH in nanowire formation, we analyzed its AlphaFold model, whose confidence scores pLDDT of most residues are above 90. *G. sulfurreducens* OscH contains two prolyl isomerase domains, PPIase 1 and 2 (**Fig. 2A & B**). In FoldSeek, the OscH model showed the highest structural homology to parvulin-type prolyl *cis-trans* isomerase. They often form dimers or homodimers, with the top part as the prolyl isomerase domain and the bottom part as the substrate-binding chaperone[48] (**Fig. 2B**). Among known examples such as *Clostridium* PrsA and *Campylobacter* Cbf2, we compared OscH to *Bacillus* PrsA because it has been extensively characterized biochemically and structurally as the sole protein known for folding secreted proteins and preventing their aggregation in Gram-positive bacteria **(Fig. S4B)**[48].

We removed its arm-like isomerase domains to evaluate the role of OscH in folding OmcS. Removal of the left arm (PPIase1 in **Fig. 2B**) significantly suppressed OmcS nanowire formation (**Fig. 2C**), causing accumulation of OmcS in the cell (**Fig. 2D**). Removal of the right arm (PPIase2) resulted in a milder defect (**Fig. 2C**). Deleting both arms (PPIase1 and 2) blocked the nanowire formation but showed some OmcS in the cell **(Fig. 2C & D)**. Thus, PPIase1 plays a more important role in nanowire formation than PPIase2. Gel shifts in OscH immunoblots confirmed the mutations and stability of truncated OscH **(Fig. 2E).** These studies further suggest that OscH helps fold OmcS into the correct conformation required for polymerization.

The OmcS contains 10 conserved prolines (green in **Fig. 2I**), which could require OscH to fold OmcS properly. Similar to OscH in the *osc* cluster, the operon of proline-rich OmcZ nanowires also encodes a prolyl isomerase (GSU2074)[20], which is essential for EET to electrodes[49]. Likely due to this OmcZ-specific prolyl isomerase, none of the *oscH* mutants inhibited OmcZ nanowire formation **(Fig. 1C, 2C)**. Thus, OscH is specific to OmcS folding, and prolyl isomerases are required for both nanowire-forming cytochromes. In contrast, *Desulfovibrio ferrophilus* OscH homolog has 16.6% protein sequence identity to OscH (**Table. S2**) and lacks PPIase1 (**Fig. 2A & S4C**). *D. ferrophilus* did not show OmcS-type nanowires when its *omcS* homolog gene upregulated, despite having the *osc* cluster[50] (**Fig. 1A, Table. S2 & S3**). This incomplete OscH and lack of OmcS-type nanowires could explain its relatively poor EET capability compared to *G. sulfurreducens*[51]

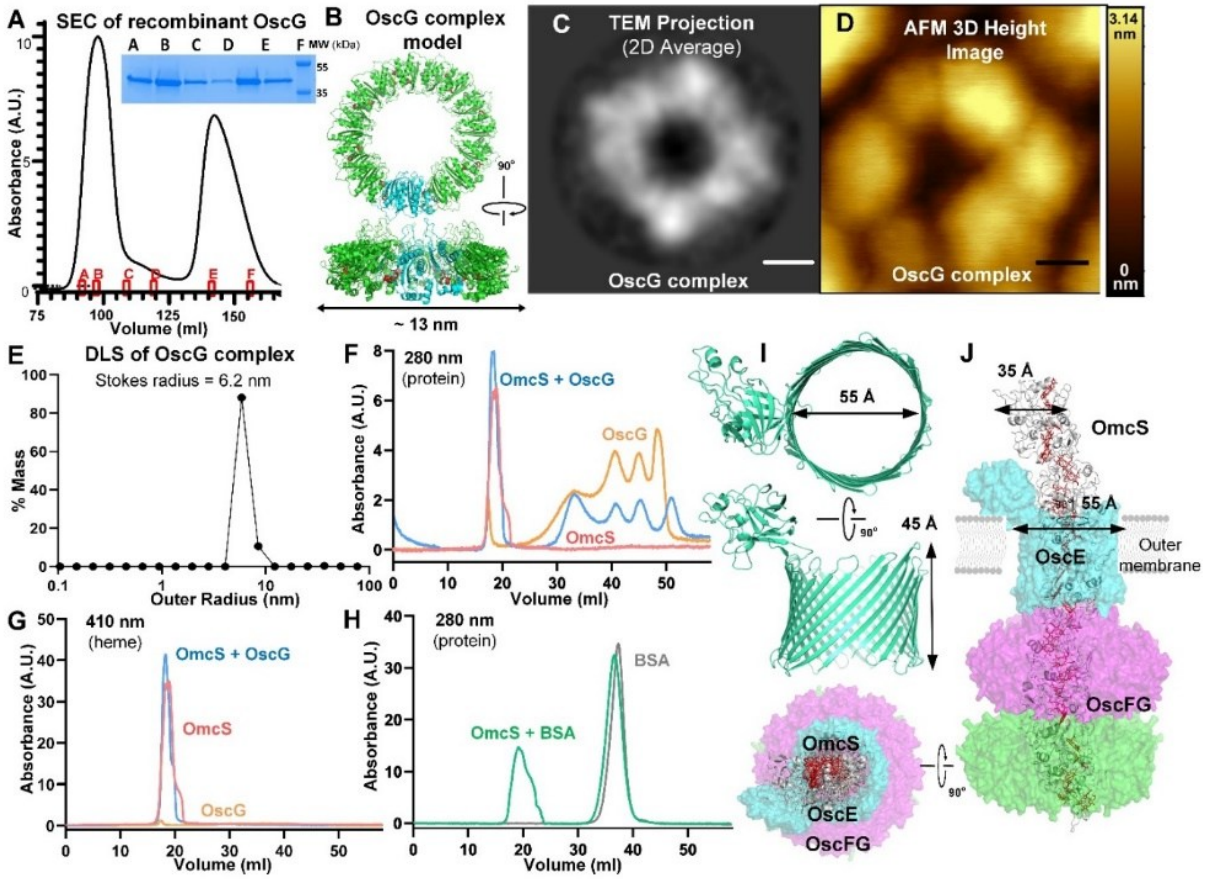

Fig. 3 OscG forms a secretion channel-like ring structure and binds to OmcS nanowires. A, Recombinant OscG purified by SEC. **Inset,** Coomassie gel of OscG from marked positions. **B,** OscG model (protomer in cyan, octamer in green) with DEAD-type motif (red). OscG ring complex was revealed by **C,** the 2D average of negative-stain TEM images, **D,** the 3D height profile from the AFM image, and **E**, the size distribution from the DLS. Scale bars, **C,** 3 nm and **D,** 20 nm. The binding of OscG complex to OmcS homolog nanowire measured by **F,** protein (280 nm) and **G,** heme (410 nm) absorbance of SEC. **H,** OmcS nanowires do not bind BSA. **I,** AlphaFold models of OscE. **J,** Simplified hypothetical model of the OscEFG channel.

To directly evaluate if OmcS binds to OscH, Strep-tagged OscH was pulled down from *G. sulfurreducens*. OmcS was the major cytochrome eluted with OscH, suggesting a specific interaction between them (**Fig. 2F-G**). Besides, treating Δ*oscH* mutants with a protease inhibitor cocktail partially prevented OmcS from degradation in Δ*oscH* cells in a dose-dependent manner, indicating that unfolded OmcS likely degraded without OscH (**Fig. 2H**). The periplasmic localization of OscH (**Fig. S5A**), where OmcS matures and accumulates (**Fig. S5F**), is also consistent with the proposed role of OscH acting as a chaperon for stabilizing OmcS within the cell.

These findings are consistent with the docking analysis showing that the OscH model holds OmcS in a rhomboid shape **(Fig. 2I)** by sliding OmcS into its central crevice. The OscH chaperone domain and PPIase arms hold the bottom and sides of OmcS tightly. This conformation exposes the polymerization interface containing His16, which coordinates heme in the neighboring subunit (cyan in **Fig. 2I**). The proximity of PPIase1 to the proline-rich regions of OmcS is consistent with its higher importance than PPIase2 in forming OmcS nanowires. Thus, OscH can act as a chaperone to stabilize the intracellular OmcS with prolyl cis-trans isomerases to fold OmcS into the correct conformation for polymerization.

OscG can form a secretion channel-like structure and binds to OmcS nanowires. Size exclusion chromatography (SEC) (**Fig. 3A**), structural modeling (**Fig. 3B**), TEM (**Fig. 3C**) & atomic force microscopy (AFM) (**Fig. 3D**) imaging, and dynamic light scattering (DLS, the measurement of Stokes radius) (**Fig. 3E**), revealed that OscG forms a ring complex with ~12 nm outer diameter (**Fig. 3C & E),** ~4.5 nm inner diameter (**Fig. 3C**), and ~3nm height (**Fig. 3D**). Native mass spectrometry showed that OscG obtained from two peaks in SEC were comprised of monomer **(Fig. S6A)** and primarily octamer **(Fig. S6B**) respectively**.** Some heptamers observed in the multimer peak could be due to the ionization of octamers **(Fig. S6B).** Notably, the predicted OscF and OscG structures are similar to the polysaccharide-exporting secretin PelC (**Fig. S7A-D**)[52]. This structural and functional similarity with known secretion channels further suggests that OscFG could form a secretion channel-like structure to export OmcS.

SEC showed that OscG can bind to OmcS nanowires (**Fig. 3F-H**). The molecular weight of OscG is ~40kDa. In contrast, the molecular weight of OmcS nanowires is megadalton, as there are typically more than 100 monomers in a micrometer-long filament. Therefore, these two proteins do not elute at the same place in the SEC column. After adding OmcS-type nanowires to the homologous OscG, its peak heights after the elution volume of 40 ml were reduced by >50%. In contrast, the nanowire peak height at 18 ml increased in both protein (280 nm) and heme (410 nm) absorbances (**Fig. 3F & G**). In contrast, another protein, bovine serum albumin (BSA), did not bind to OmcS-type nanowires (**Fig. 3H**), confirming OscG-specific nanowire binding.

To evaluate the *in vivo* interaction of OscG to OmcS, we performed a pull-down of His-tagged OscG from *G. sulfurreducens*. OmcS was enriched in the elution of OscG only for induced cells **(Fig. S8A & B)** and did not bind to the affinity column by itself (**Fig. S8C**). The presence of OmcS was confirmed by immunoblots and heme staining **(Fig. S8D & E)**, suggesting OscG interacts with OmcS *in vivo* in agreement with *in vitro* studies (**Fig. 3F-H**). The band shift between the immunoblot and the heme staining came from the addition of the reducing reagent β-mercaptoethanol (**Fig. S8F**).

OscEFG could potentially form a secretion channel-like structure for OmcS nanowires. OscG and OscF are mainly distributed both in the inner membrane fraction and the periplasmic fraction (**Fig. S5B & C**). The membrane and periplasmic controls confirmed a lack of contamination in subcellular fractions (**Fig. S5G-H**). Despite similar structural models to

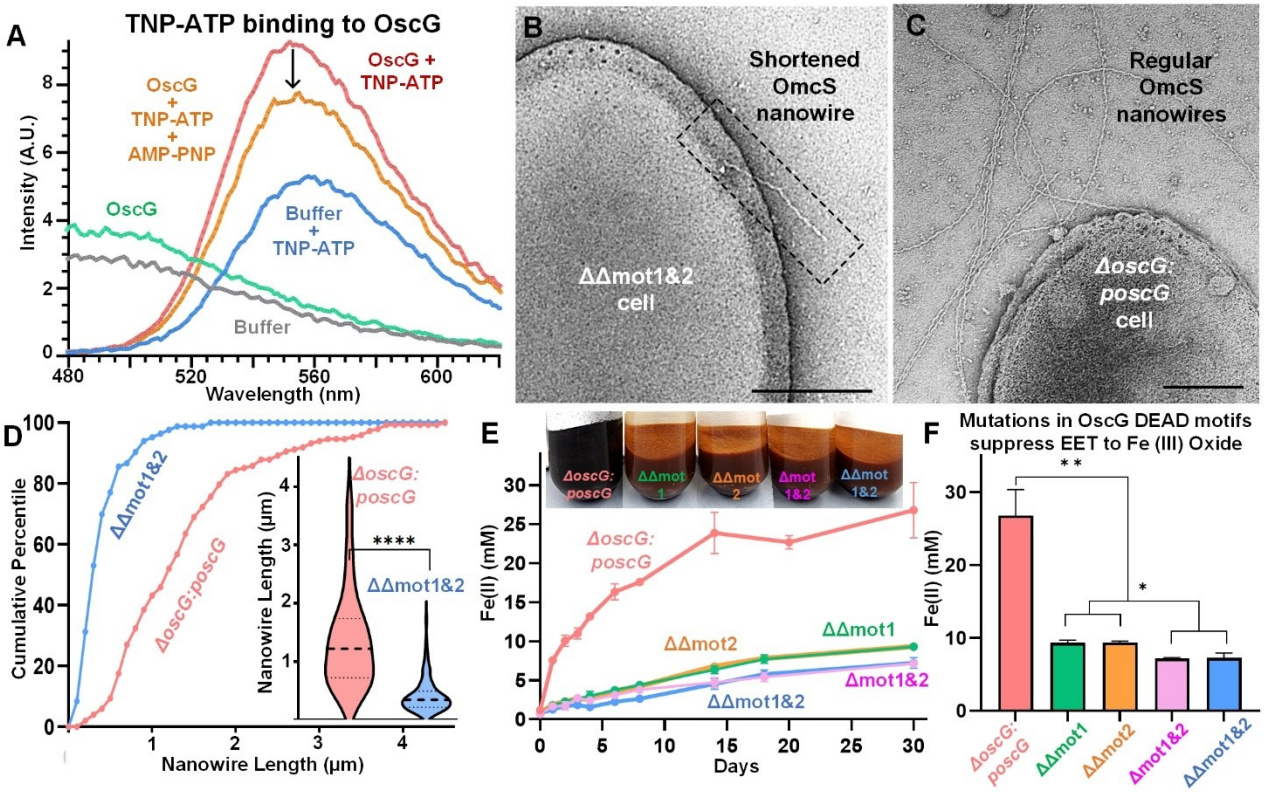

Fig. 4 OscG binds to ATP and its mutated DEAD-type motifs suppress EET and exhibit shorter cell-attached OmcS nanowires. A, Changes in the fluorescence emission showing OscG binding to the ATP fluorescent analog TNP-ATP, and non-hydrolyzable ATP analog AMP-PMP replacing this binding. Mutations in OscG DEAD-motifs shorten cell-attached OmcS nanowires as indicated by TEM images of **B,** ΔΔmot-1&2 vs. **C,** cells with WT *oscG*, scale bars, 100 nm, and **D,** cumulative length distribution (*p <0.05, **p<0.005, ****p<0.00001, Kolmogorov-Smirnov test). **Inset,** violin plot. Dotted lines in the violin plot: 25% percentile, median, and 75% percentile, respectively. n=83 for the mutant and 148 for the control. Mutations in OscG DEAD-motif suppress EET to Fe(III) oxide as revealed by **E,** time course (**inset**, unchanged cultures' color) and **F,** Day 30 measurements. Yeast extract is used as the reducing reagent for Fig. 4E&F.

PelC, the charge distributions of OscG and OscF are different (**Fig. S7G-I**). Biofilm formation requires the highly electronegative PelC ring surface to attract cationic exopolysaccharides PEL towards its pore and funnel it towards the transmembrane β-barrel domain of PelB[52]. In contrast to PEL, OmcS lacks large cationic regions and is unlikely to be secreted solely using electrostatics. This charge difference could account for the necessity of the *osc* components for the secretion of OmcS nanowires. We further found that the predicted β-barrel protein OscE (**Fig. 3I**) is in the outer membrane fraction (**Fig. S5D**). Subcellular localizations (**Fig. S5**), together with structural models of OscFG (**Fig. 3B, Fig. S7A-F**) and OscE (**Fig. 3I**), suggest a potential model for nanowire secretion with OscE embedded in the outer membrane, and OscF and OscG beneath OscE (**Fig. 3J**), as they can be found in the periplasm **(Fig. S5)**. The predicted diameter of OscE (55 Å) and the measured inner diameter of the OscG rings (45 Å) are large enough to pass nanowires (OmcS diameter ~ 35 Å) (**Fig. 3J**).

Mutated DEAD-type motifs of OscG lead to cells shortening nanowires and lowering EET. Despite similar OscF and OscG structural models, only OscG shows the DEAD-type motifs, a characteristic of some helicases with ATPase ability[53] (**Fig. 3B**), and this motif is conserved among OscG homologues across several phyla (**Table. S5**). Fluorescence spectroscopy revealed that upon binding to OscG, the fluorescent peak emission of the ATP fluorescent analog TNP-ATP increased almost 2-fold and blue-shifted by ~7 nm as expected[54] (**Fig. 4A**). Displacing TNP-ATP by the non-hydrolyzable ATP analog AMP-PNP[54] lowered the emission intensity, confirming that the fluorescence is due to ATP specifically binding to OscG. Notably, native mass spectrometry revealed that ATP analog binding induces oligomerization of OscG into dimers and trimers (**Fig. S6C & D**), and monomer OscG exhibited a significant shift and a narrower distribution in charge states (**Fig. S6E**), suggesting a more compact and well-folded conformation[55].

To evaluate the role of OscG DEAD-type motifs in nanowire formation, we substituted alanine with the acidic residues critical for hydrolyzing ATP[56] in the motif-1: DEAD (#76-79) and motif-2: EELE (#383-386) as follows (**Table S6**): ΔΔmot1 (**AA**AD & EELE), ΔΔmot2 (DEAD & **AA**LE), Δmot1&2 (**A**EAD & **A**ELE) ΔΔmot1&2 (**AA**AD & **AA**LE). Point mutations of these two residues (DE) abolish the ATP hydrolysis, but not the ATP binding ability and the stability or expression of the protein[56]. Mutating DE to EE does not affect the ATP binding and ATP hydrolysis[56]. Notably, surface-displayed OmcS nanowires were shorter in mutated *oscG* cells than wild-type *oscG* (**Fig. 4B-D**) in liquid cultures where EET is not essential for bacterial growth. Furthermore, the mutated OscG significantly suppressed the EET to Fe(III) oxide **(Fig. 4E & F)**, which was also evident in their inability to alter the culture color from brown to black (**Fig. 4E inset**). Cells with both motifs mutated had lower EET ability than those with only one motif mutated, suggesting the involvement of both motifs in the reduction of Fe(III) oxide (**Fig. 4E & F**). As nanowires need to bind to Fe(III) oxides during EET, shorter nanowires can cause less Fe(III) oxide binding, leading to lower EET. Thus, OscG and its DEAD-type motifs lead to cells producing shorter OmcS nanowires and lowering EET to Fe(III) oxide in an ATP-dependent manner. The inner membrane fraction of OscG **(Fig. S5B)** could allow ATP binding at the cytoplasmic side of the inner membrane.

Cells with OscG lacking ATP-hydrolyzing motifs only have a partial loss of function on the OmcS nanowire assembly and EET but do not completely inhibit it. Upon mutations of ATP-hydrolyzing motifs on OscG, bacterial cells did not lose the ability of OmcS nanowires formation (**Fig. 4B&D**) and were still capable of EET ability to iron oxide (**Fig.4E&F**), whereas Δ*oscG* cells cannot assemble any OmcS nanowire (**Fig. 1C&G**) and inhibited the EET ability to iron oxide (**Fig. 5C&D**). These physiological data indicate that these mutated OscG are still expressed and stable. Otherwise, we would not have seen any nanowire assembly or significant iron oxide reduction due to EET.

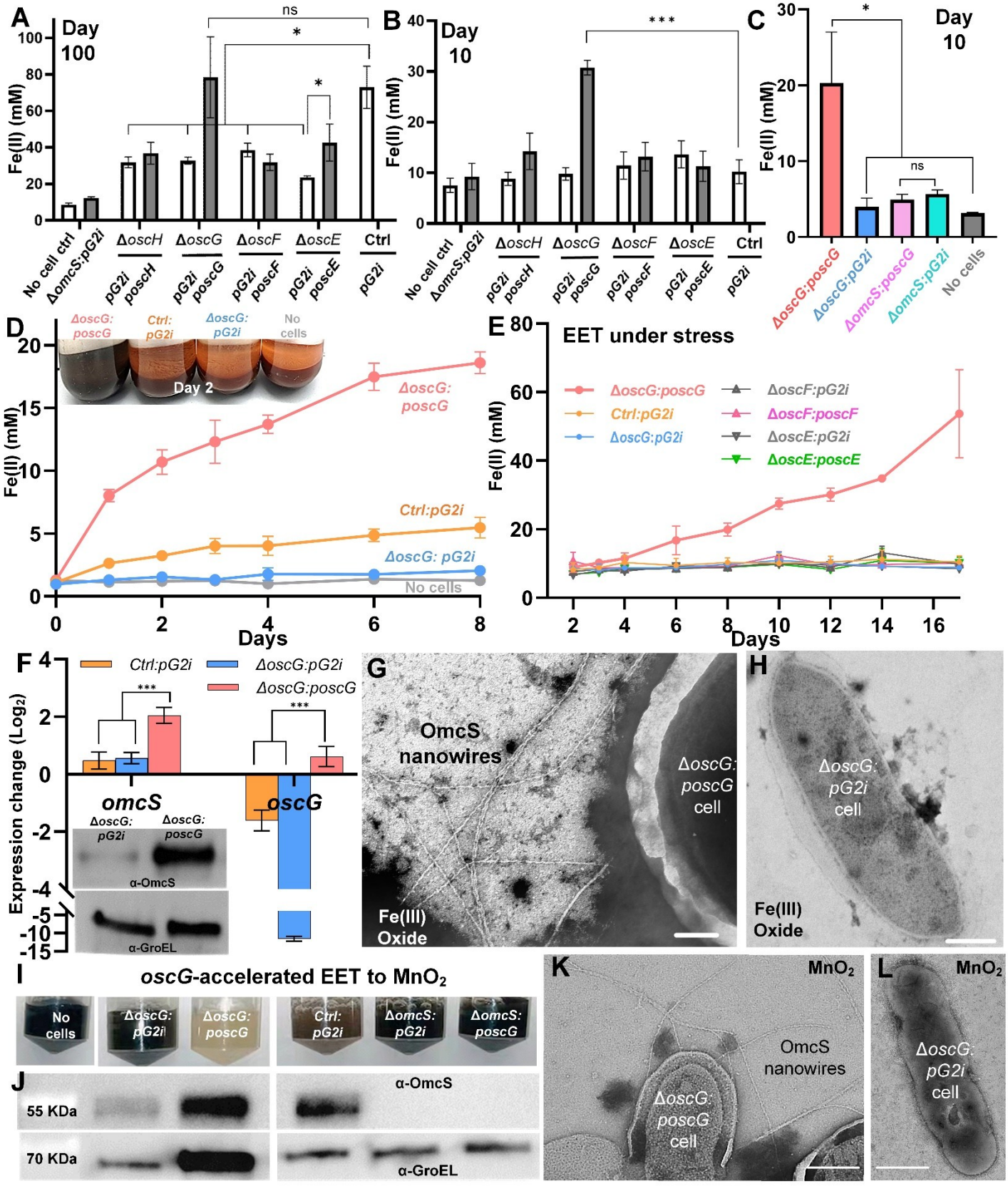

Fig. 5 *oscG*-complemented cells accelerate EET to Fe(III) oxide and MnO_2 in an *omcS*-dependent way. A, Δ*oscE,* Δ*oscF,* Δ*oscG* and Δ*oscH* showed a defect in EET to Fe(III) oxide at day 100. **B-E**, *oscG*-complemented cells accelerated initial growth on Fe(III) oxide: **B**, at day 10, **C,** expressing *oscG in trans* in Δ*omcS* did not accelerate EET at Day 10. **Inset in D**, Fast color change of iron oxide culture. Stress conditions in **E**, antibiotic (200 μg/ml kanamycin) and inducer (500 μM vanillate). EET acceleration is due to *oscG*-complemented cells **F,** overexpressing *omcS* gene in liquid culture, **inset**, overproducing OmcS at protein level, and **G,** forming more OmcS nanowires than **H,** control as revealed by TEM images in iron oxide cultures. EET acceleration to MnO_2 by *oscG*-complemented cells are shown as **I,** a faster color change from oxidized black into reduced white within 20 days, **J,** overproduction of GroEL protein at day 60 and **K**, more OmcS nanowires vs. **L**, control from TEM images. All error bars, SD. Biological replicates n=3 for **A,B** and **E**, n=4 for **C, D and F**. *p <0.05, ***p<0.005. GroEL, cellular control and is used as a proxy for the cell amount. Cysteine is used as the reducing reagent for **A**, **B** & **E** and leads to the elevated level of Fe(II) at Day 0. Yeast extract is used as the reducing reagent for **C** & **D** and minimize the reduction of Fe(III) at Day 0.

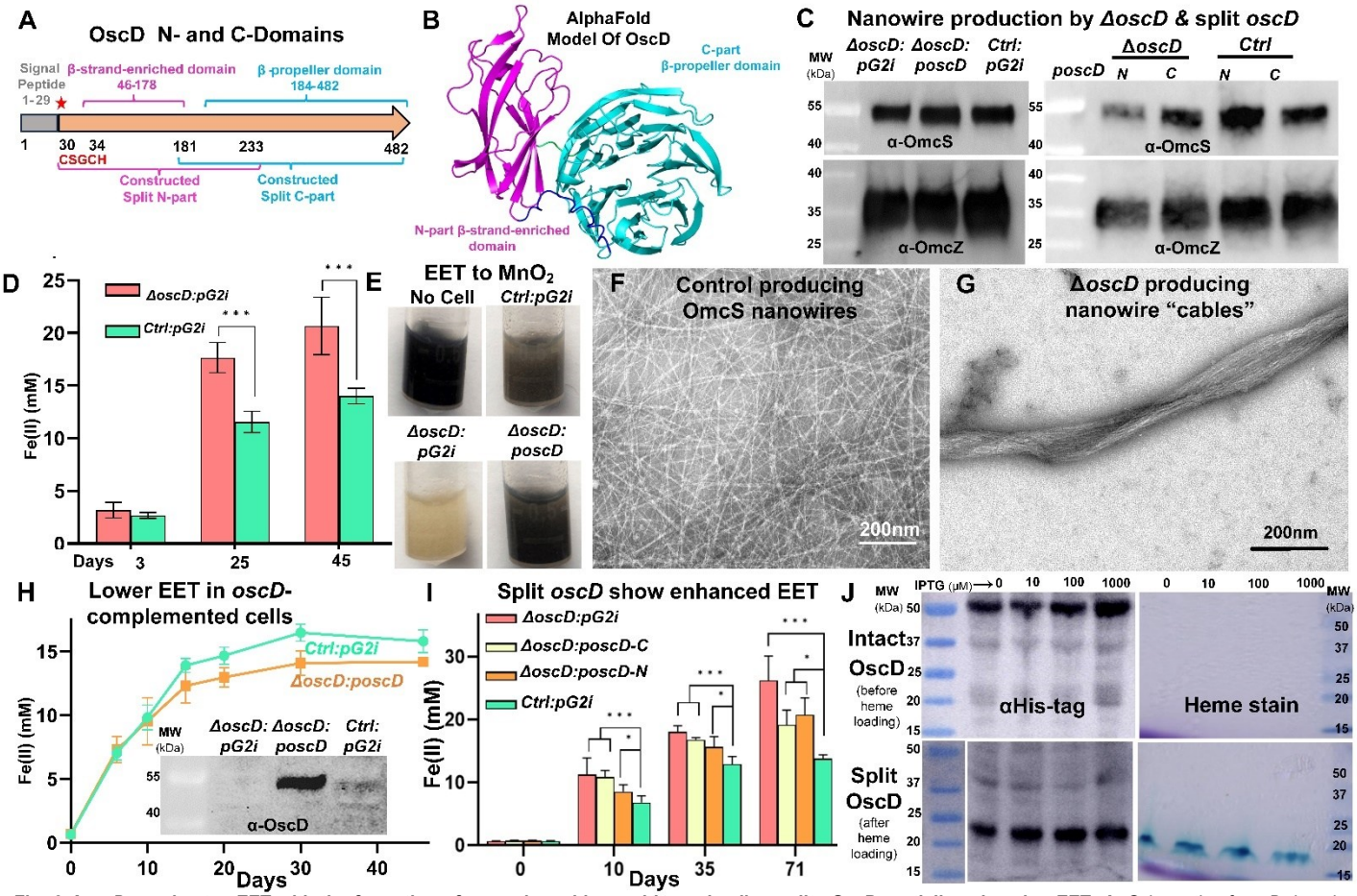

Fig. 6 *ΔoscD* accelerates EET with the formation of nanowire cables and heme loading splits OscD partially enhancing EET. A, Schematic of *oscD* domains showing split regions and the location of the heme-binding motif (highlighted in red). **B,** AlphaFold model of OscD structure shows N-terminal flexible stretch (blue), N-part β-sheet-enriched domain (pink) and C-part β-propeller domain (cyan). OmcS nanowires were formed by **C**, Δ*oscD*, and *oscD*-complemented cells (left) and cells with split-*oscD* with N- and C-part expressed separately (right). **D-E**, Δ*oscD* cells performed faster EET to **D,** Fe(III) oxide and **E,** MnO_2 at day 25. OmcS nanowires **F,** form individually in the filament fraction of the *Ctrl* cells and **G,** form as cables by Δ*oscD* cells grown with Fe(III) oxide. **H,** *oscD*-complemented cells performed slightly slower EET to Fe(III) oxide than the *Ctrl* cells. (**Inset)** Immunoblot shows higher OscD amount from *oscD*-complemented cells in liquid culture. **I,** Cells with split-*oscD* accelerated EET to Fe(III) oxide faster than the *Ctrl* cells but slower than full-length *oscD*. **J,** Recombinant OscD contains heme-binding motif at N-terminal and His-tag at C-terminal. Immunoblots and heme-staining gels show that, **top**, heme-free OscD: intact full-length (~50 kDa, left) and no detected heme signal (right); **bottom**, heme-loaded OscD: split OscD with His-tag at C-part (~25 kDa, left) and split OscD with loaded heme at N-part (~20kDa, right). All error bars, SD, n=4 biological replicates, *p <0.05, ***p<0.005.

***oscG*-complemented cells accelerate EET, but only in the presence of *omcS*.** OmcS was shown to be essential for metal oxide reduction[32]. Therefore, EET to metal oxides was chosen to study the rate of OmcS-mediated EET. The *osc* mutants that lack OmcS nanowires have defects in EET to Fe(III) oxide, confirming that OmcS nanowires are essential for EET (**Fig. 5A**). Complemented *oscF and oscH* did not restore the growth, possibly due to less plasmid activity over 100 days (**Fig. 5A**).

Remarkably, *oscG*-complemented cells grew rapidly (**Fig. 5B-E**) as the Fe(III) oxide media turned from oxidative brown to reductive black within two days **(Fig. 5D, inset**). Rapid growth was more apparent under stress conditions of high antibiotic and inducer concentrations (**Fig. 5E**). Expressing *oscG* in Δ*omcS* cells did not accelerate EET to Fe(III) oxide, confirming that the rapid EET is *omcS*-dependent (**Fig. 5C**). Upon complementation of *oscG*, the transcriptional level of *omcS* elevated 3-fold compared with *Ctrl:pG2i* strain (**Fig. 5F**). Cell lysates, instead of filament fractions, were used for biochemical analyses of mineral cultures due to low cell density and slow growth. Immunoblots revealed that *oscG*-complemented cells overproduced OmcS protein in iron oxide cultures (**Fig. 5F, inset**), and TEM images confirmed that OmcS nanowires connected these cells to minerals (**Fig. 5G & H**). The *oscG*-complemented cells also accelerated EET to MnO_2, which correlated with the production of OmcS nanowires (**Fig. 5I-L**). Cells turned oxidized black culture into reduced white culture in an *omcS*-dependent way. This *omcS*-dependent EET acceleration by OscG further indicates that ATP-bound OscG can promote the formation of OmcS nanowires.

The lack of OscD accelerates EET with bundling nanowires into cables. OscD, located in the outer membrane (**Fig. S5E**), contains two major domains: An N-part β-sheet enriched domain and a C-part β-propeller domain with a heme-binding motif (CSGCH) as the first five amino acids (**Fig. 6A, B**). To probe the role of OscD, we expressed the OscD and its domains separately into Δ*oscD* cells and the *Ctrl* cells (**Fig. 6C**). Neither the deletion nor complementation of OscD affected the formation of nanowires (**Fig. 6C**). Surprisingly, Δ*oscD* accelerated EET to Fe(III) oxide (**Fig. 6D**) and MnO_2 (**Fig. 6E**). TEM imaging revealed that the morphology of OmcS nanowires in these cells was changed from individual filament (**Fig. 6F**) to cable-like bundles whose width are more than 40 nm (**Fig. 6G**). Therefore, EET acceleration could be due to cells forming cables to increase the nanowire density for more efficient binding and reduction of minerals. The *oscD*-complemented cells overproduced OscD (**Fig. 6H, inset**) and showed EET similar to the wild-type (**Fig. 6D & H**).

Heme loading splits OscD, rendering it less functional. The complementations of individual OscD domains exhibited higher EET than the *Ctrl* cells but lower than Δ*oscD* (**Fig. 6I**). Cells thus only need to eliminate a single OscD domain to accelerate EET. To probe how cells could use OscD to tune the EET rate, we reconstituted OscD in *Escherichia coli*. Surprisingly, the heme loading led to the cleavage of OscD into separate N- and C-part (**Fig. 6J**). The binding of hemes can inactivate some proteins to regulate various physiological processes. For example, upon binding to heme, the bacterial iron response regulator (Irr) protein[57] and the transcription repressor Bach1[58] rapidly degrade because this

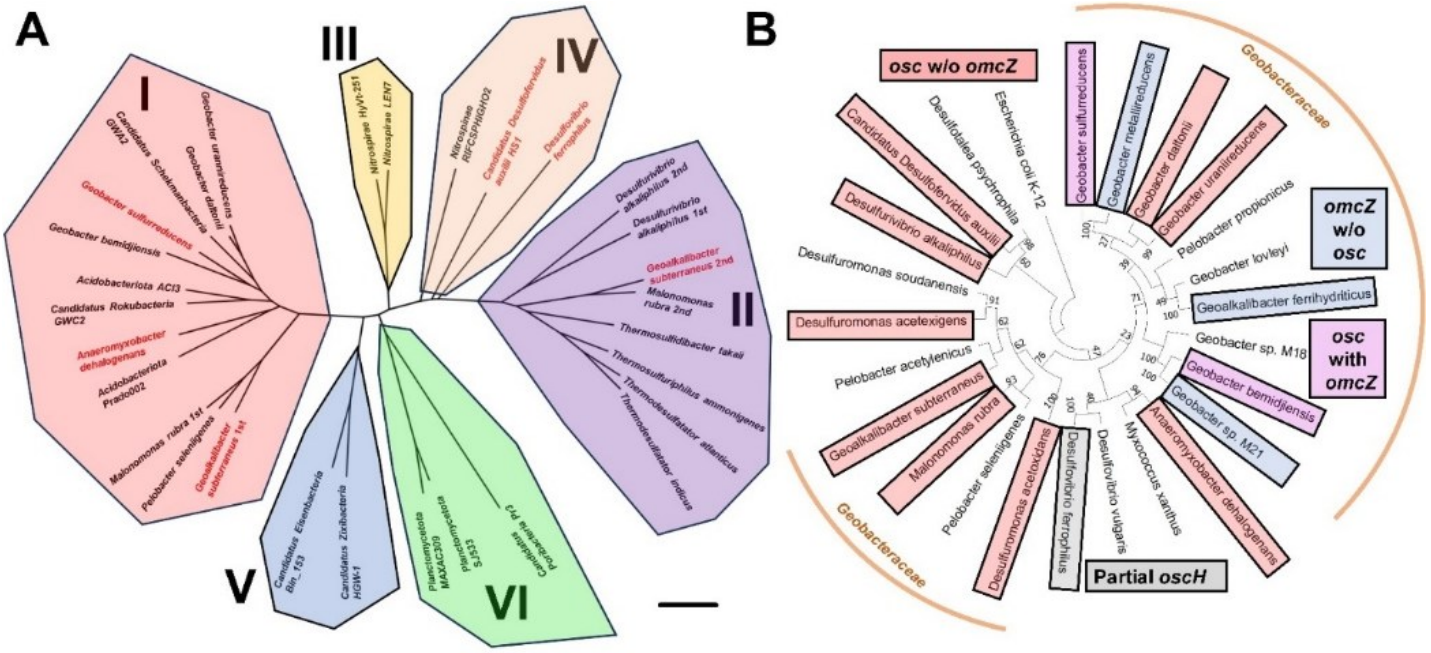

Fig. 7 OmcS nanowire assembly machinery is widespread and ancient. A, Phylogenetic tree derived from concatenated protein sequence alignments (OscEFGH) showing clades I-VI. Species discussed are in red. Scale bar, 0.5. **B,** Phylogenetic tree, based on housekeeping gene *recA,* shows that the *osc* cluster (red) exists in a part of *Geobacteraceae* family and its closely-related bacterial species. The *osc* cluster (orange) is also more widespread than *omcZ* (blue) among bacteria, with only two species showing both OmcS and OmcZ nanowires (pink). The species with partial OscH was highlighted in grey.

binding can change their conformation or produce local reactive oxygen species that facilitate proteolytic cleavage[57]. *G. sulfurreducens* could adopt a similar strategy of heme-induced cleavage, thereby promoting the formation of nanowire cables and accelerating the EET.

OmcS nanowire assembly machinery is widespread and ancient. Most bacterial species that contain the *osc* cluster grow in anoxic conditions by reducing sulfate or metal oxides. They form six clades based on the phylogeny tree of the core components OscEFGH, with a significant number of them remaining uncultivated (**Fig. 7A**). Clade I is mesophiles inhabiting soils and sediments[9] (**Fig. 7A, left**). Clade II is thermophiles living in marine sediments and hydrothermal vents[2] (**Fig. 7A, right**). Clade IV includes DIET-performing Candidatus *D. auxilii*[54]. In contrast, other Clades are detected mainly by metagenomics from various environments, such as groundwater, soil, and bioreactors[59,60] (**Fig. 7A, middle**).

The *osc* cluster exhibits sporadic distribution in the phylogenetic tree based on the housekeeping gene *recA* (**Fig. 7B**). OmcS homologs are more widely distributed in bacteria than OmcZ homologs. Still, within the *Geobacteraceae* family, not all genomes contain OmcS homologs (**Fig. 7B**). Although this distribution suggests that OmcS nanowires and the *osc* cluster may be acquired via horizontal gene transfer, we found that the GC (guanine-cytosine) content of the *osc* cluster exhibits no difference from the corresponding genome backgrounds, even for species with genomic GC >70% (*A. dehalogenans*) or <40% (HotSeep-1) (**Fig. S1B**). Many Clade II species, such as *Thermosulfidibacter*[61] and *Thermodesulfatator*[62] are thermophilic, anaerobic, hydrogen-dependent chemolithoautotrophic bacteria inhabiting deep-sea hydrothermal vents. These conditions are reminiscent of the proposed living conditions for the last universal common ancestor that existed ~4 billion years ago[63]. Furthermore, thermophiles on early Earth are proposed to be capable of EET to Fe(III) oxide[64]. Thus, the Osc machinery-based nanowire assembly has an ancient origin and has evolved to survive via EET in diverse species and environments.

Conclusions. Combining molecular biology, biochemistry, biophysics, and imaging methods, our study identifies the machinery required to form OmcS nanowires. We show that the folding chaperon OscH is required for the biogenesis of the intracellular OmcS, the porin OscE, and the channel-like protein OscF & OscG are necessary for the nanowire secretion, and OscD is important for maintaining the morphology of OmcS nanowires. By demonstrating that inhibition of OmcS nanowires formation suppresses EET and that higher abundance or aggregation of OmcS nanowires accelerates EET, our work also establishes the physiological role of OmcS nanowires in EET. The *oscG*-complemented cells not only accelerate EET to insoluble Fe (III) oxide, but also to soluble Fe (III) citrate[65]. Besides, we find that the nanowire assembly machinery is ancient and widespread.

Other proteins in the *osc* cluster could also be involved in the formation and function of OmcS nanowires. For example, the disruption of *oscA* diminished the current production when cells were cultured on graphite electrodes in the first 60 hours[66], consistent with the role of the *omcST* operon during the early stage of biofilm growth on electrodes[34]. We found that Δ*omcS* cannot adapt to grow on iron oxide even after 100 days, consistent with prior studies[32,35]. However, one study reported adaptation after 40 days with Δ*omcS* showing mutations on two regulator genes (GSU1771 and GSU2507). ΔGSU1771 is known to overproduce OmcS and other cytochromes[67]. Notably, GSU2507 is near *oscA* (GSU2505) and *omcS* (GSU2504), further suggesting the role of the *osc* cluster in EET. The adaptation of this Δ*omcS* could be due to OmcS paralog proteins (OmcT, OmcJ, and OscC) compensating for the loss of OmcS, where further studies are required.

DIET-performing co-cultures, comprised of anaerobic methanotrophic archaea (ANME) and sulfate-reducing bacteria, overexpress multi-heme cytochrome during methane oxidation[2,3,68]. However, the identity of these overexpressed cytochromes remained unclear. Our analysis reveals that some of these cytochromes are in fact OmcS homologs. For example, Hotseep-1 (HS1) overexpresses 3 OmcS homologs (gene locus: 002099[2]/RS03280, RS00830, RS03285[69]) by ~10-fold during methane oxidation. Therefore, OmcS-type cytochrome nanowires could be enabling rapid methane oxidation. Our findings could also help biocatalysis applications. For example, cyanobacteria expressing monomeric OmcS show 10-fold higher photocurrent[70] and nitrogen fixation[40] and 60% higher biomass for improved photosynthesis[39]. The heterologous expression of *osc* cluster to assemble OmcS nanowires could further improve their performance.

The use of cytochrome-based nanowires could be more widespread because most microbes still cannot be cultured and systematically studied in the lab. Therefore, we expect that the molecular mechanisms discovered in this work can serve as a blueprint to discover other microbes that can form OmcS-type nanowires for various physiological and ecological functions. Besides, the heterologous expression of the *osc* machinery could potentially engineer EET capability into environmentally, clinically, and commercially important microbes so that they can metabolize rapidly across distances spanning hundreds of micrometers. OmcS-type nanowires thus could be applied to improve the microbial performance for bioenergy and biocatalysis applications that rely on conventional EET but show poor performance due to the slow diffusion of small molecules interfacing bacteria with electronics. Furthermore, as microbial nanowires are important materials for bioelectronics[71,72], these design principles can be applied to developing new synthetic biology toolboxes to engineer on-demand nanowire assemblies with tunable electronic and ionic conductivity[72].

Limitations of the study. Here we have focused on genetic, biochemical, physiological and structural modeling approaches to identify nanowire assembly machinery. Future studies using advanced structural and biophysical approaches, such as cryo-electron tomography, are necessary to elucidate the assembly architecture and mechanism in further detail.

Significance. Microbial respiration via extracellular electron transfer (EET) drives various globally important environmental processes such as biogeochemical cycles of metals and greenhouse gases. It has biotechnology applications for bioenergy, bioremediation, and bioelectronics, such as sensing environmental contaminants and controlling pathogen growth. EET via surface-displayed polymerized cytochrome “nanowires” has been proposed to be ubiquitous in prokaryotes. This assumes that cytochromes with conserved heme stacking can polymerize into conductive filaments and are used for EET. However, most microbes cannot perform EET, and most cytochromes cannot polymerize despite conserved heme stacking. Here, we show that a conserved *omcS*-companion (*osc*) cluster drives the formation of OmcS cytochrome nanowires in *Geobacter sulfurreducens*. This finding is significant because among 111 cytochrome genes in *G. sulfurreducens*, OmcS is the only known nanowire-forming cytochrome essential for EET to minerals abundant in subsurface environments. In contrast to the long-held view that OmcS transfers electrons to pili “nanowires,” we find that cells directly use OmcS nanowires for EET to minerals. Our work thus resolves a long-standing controversy about the physiological function of microbial nanowires. Furthermore, we show that this modular biosynthetic gene cluster assembles cytochrome OmcS into nanowires, enabling accelerated EET by stimulating nanowire production and bundling nanowires into cables. These design principles can be applied to developing new synthetic biology strategies to rationally engineer nanowires with tunable electron conductivity to accelerate EET in diverse microbes to overcome the limitations of slow, electron shuttling via diffusible, redox molecules. Our finding of a single gene cluster being crucial to assemble nanowires that confer long-range EET capability to microbes is a significant improvement over current approaches that typically require incorporating multiple electron-transferring systems and achieving only short-range (< 1 μm) EET due to the lack of nanowires. Therefore, this previously undescribed nanowire assembly strategy could help improve EET in diverse species and environments.

RESOURCE AVAILABILITY

Lead Contact

Further information and requests for resources and reagents should be directed to and will be fulfilled by the Lead Contact, Nikhil S. Malvankar (Nikhil.malvankar@yale.edu)

Materials Availability Statement

Materials generated in this study will be made available on request, but we may require a payment and/or a completed Materials Transfer Agreement if there is potential for commercial application.

Data and Code Availability

- All data reported in this paper will be shared by the lead contact upon request.
- This paper does not report the original code.
- Any additional information required to reanalyze the data reported in this paper is available from the lead contact upon request.

ACKNOWLEDGMENT

We thank A. Goodman, C. Roy, J. Liu, G. Brudvig, F. Olivera, R. Jain, and E. Martz for discussions; A. Sui, J. Mendens and other staff from Yale West Campus Research Support Services for medium preparation and logistics support; D. Bond for providing the plasmids and genetic protocols; D. Lovley, K. Inoue for providing bacteria strains; S. Umlauf for help with fluorescence measurements; J. Kanyo for mass spectrometry data analysis; C. Zhang for the guidance on structure modeling and comparison; the Biophysics Resource of Keck Laboratory at Yale School of Medicine for DLS; W.M. Keck Foundation Biotechnology Resource Laboratory for mass spectrometry; Yale West Campus Imaging Core for AFM and TEM imaging; Yale Center for Genome Analysis for whole genome sequencing and analyses of in-frame deletion mutants; Yale Center for Molecular Discovery for fluorescence intensity measurements. This research was supported by the National Institutes of Health Director's New Innovator award (1DP2AI138259-01 to N.S.M. and R01GM141192 to K.G.), the Human Frontier Science Program award (no. RGP017/2023 (to N.S.M) and US National Science Foundation (NSF) CAREER award no. 1749662, NSF-ANR award no. 2210473 (to N.S.M.) and the Department of Energy award no. DE-SC0025520 (to N.S.M.).

AUTHOR CONTRIBUTIONS

C.S. and N.S.M. designed the project. C.S. performed bioinformatic analyses, bacterial growth, RT-PCR, qRT-PCR, negative-stain TEM, AFM imaging, purification of OmcS-homolog filaments from *G. subterraneus*, genetic constructions, biochemical analyses, iron oxide reduction, manganese oxide reduction, subcellular fractionation, purification of recombinant proteins from *E.coli,* SEC, fluorescence spectroscopy, DLS and AlphaFold models and analysis on OscH. A.I.S.-M. conducted TEM imaging, iron oxide reduction assay, and immunoblots on *ΔoscH* treated by protease inhibitors. W.J. performed native mass spectrometry and its analyses under K.G.’s supervision. J.E. helped with qRT-PCR measurements and protein purification. Y.G. conducted TEM imaging and 2D averaging of recombinant OscG. A.C. helped with the iron oxide reduction assay. S. E. Y. performed AFM imaging of recombinant OscG. F.A.S. purified recombinant proteins from *E. coli* and built AlphaFold models. N.S.M. supervised the project. C.S. and N.S.M. wrote the manuscript with input from all the authors.

DECLARATION OF INTERESTS

The authors declare no competing interests.

STAR★METHODS

Detailed methods are provided in the online version of this paper and include the following:

- KEY RESOURCES TABLE
- EXPERIMENTAL MODEL AND STUDY PARTICIPANT DETAILS
  - Bacterial strains and culture
- METHOD DETAILS
  - Bioinformatic analyses
  - Reverse transcription-PCR (RT-PCR) and quantitative RT-PCR (qRT-PCR)
  - Genetic manipulation
  - Nanowire purification
  - Sodium dodecyl sulfate–polyacrylamide gel electrophoresis (SDS-PAGE) and heme staining gels
  - Mass spectrometry for the filament fraction
  - Negative staining transmission electron microscopy (TEM)
  - Atomic force microscopy (AFM) imaging
  - Bacterial growth with Fe(III) oxide and MnO2
  - Subcellular fractionations
  - Immunoblotting and antibody characterization
  - Pull-down of OscH and OscG
  - Proteinase inhibitory assay
  - Recombinant protein purification
  - Native mass spectrometry
  - Dynamic light scattering (DLS)
  - Fluorescent spectroscopy
  - Protein interactions with OmcS-type nanowires
  - AlphaFold predictions and analyses on structural models
- QUANTIFICATION AND STATISTICAL ANALYSIS

SUPPLEMENTAL INFORMATION

Supplemental information can be found online.

EXPERIMENTAL MODEL AND STUDY PARTICIPANT DETAILS

Bacterial strains and culture. *Geobacter sulfurreducens* strains PCA (the wild type, denoted as WT), CL-1 (ΔGSU1240 on lab PCA strain background, denoted as the *Ctrl* strain in this study)[46] . We chose CL-1 as the control strain because it routinely produces OmcS nanowires in NBAF liquid medium[17]. The *Ctrl* strain expressed *omcS* over 3-fold (Fig. S2C) and ~7-fold more than WT at exponential and stationary phase, respectively (Fig. S2D), while other *osc* genes did not show noticeable differences. Plasmid disruption, in-frame deletion mutants (*oscD*, *oscE*, *oscF*, *oscG*, *oscH*, and omcS), their complementations, truncations, and point mutations are constructed in this study based on CL-1 strain. As previously described[17,22], all *G. sulfurreducens* liquid cultures were kept in sterilized and degassed NBAF medium at 30 °C under strictly dark and anaerobic conditions. 15 mM acetate was used as an electron donor, 40 mM fumarate was used as an electron acceptor, and 1 mM cysteine was added as an oxygen scavenger.

METHOD DETAILS:

Bioinformatic analyses. The *osc* clusters in other bacteria were analyzed by searching Osc proteins from *G. sulfurreducens* with Position-Specific Iterative Basic Local Alignment Search Tool (PSI-blast)[73] of 4-iterations against NCBI Non-Redundant database (NR). Homologs of other *osc* components were confirmed by protein Blast (blastp). Selection of protein homologs follows the criteria that alignment coverages are above 70%, and e-values are smaller than 1e-20. The protein phylogeny tree of concatenated OscEFGH and the nucleic acid phylogeny tree of housekeeping gene *recA* were constructed by the maximum likelihood method with Mega-X[74] and presented by iTOL[75]. Gene expression data in Fig. 1c were analyzed and summarized from transcriptome data of previous publications for the following growth conditions: iron oxide vs iron citrate[76], Δ*omcB* vs WT[77] and Δ*cheR5* vs WT[78]. In addition, we analyzed transcriptome data for HotSeep-1 under DIET conditions[2]. Signal peptide predictions were conducted by SignalP 5.0[79]. The statistical significances were calculated using the Student's t-test when not specified.

Reverse transcription-PCR (RT-PCR) and quantitative RT-PCR (qRT-PCR). For RT-PCR, 20 ml late-exponential *G. sulfurreducens Ctrl* cells were harvested, saved in RNAprotect Bacteria Reagent (QIAGEN), and frozen at -80 °C. Cells were lysed by 200 µl TE buffer pH 8.0 supplemented with 320 ug/ml lysozyme and 100 µg/ml proteinase K. RNeasy Mini Kit (Cat. No. 74104, Qiagen) was applied for RNA extraction. Contaminant DNA was removed by a TURBO DNA-free kit (Cat. No. AM1907, Invitrogen). SuperScript First-Strand Synthesis System synthesized cDNA first strand for RT-PCR kit (Cat. No.11904018, Invitrogen). To probe the operon structure of the *osc* cluster, the intergenic regions of the *osc* cluster from genomic DNA, cDNA from extracted RNA, and no reverse transcriptase control were amplified by PCR. For qRT-PCR, the cDNA was amplified by KAPA SYBR FAST qPCR Kit Master Mix (2X) (KK4605, Roche) following the protocol: initial melting 95 °C, 3min; then 40 cycles of 95 °C, 3s and 60 °C, 30s. The primers for qRT-PCR were chosen close to the 3' end of target genes with a length of 120-150bp. The fluorescence signals were measured and quantified by CFX Opus 96 Real-time PCR system (Bio-Rad). The exponential phase was chosen when the optical cell density at 600 nm absorbance (OD_{600}) was ~ 0.4. The stationary phase was chosen when OD_{600} was saturated at ~0.7 for 6 hours.

Genetic manipulation. Plasmid pk18mobsacB (pk18) was used for plasmid disruption[80] and in-frame deletion[81]. For plasmid disruption, approximate 500 bp central regions of *oscD*, the intergenic region between GSU2390 and GSU2391, and the intergenic region between GSU2591 and GSU2592 were cloned and ligated to pk18mobsacB. *E. coli* S17 strain[82] was used to conjugate the constructed plasmid into *G. sulfurreducens* strain CL-1. The homolog regions of both *the G. sulfurreducens* chromosome and pk18mobsacB plasmid led the integration of the plasmid into target genes on the chromosome. Mutants were maintained with 200 µg/ml kanamycin for single homologous recombination. For in-frame deletion, the flanking regions of *oscD-H* and *omcS* were joined and ligated to pk18mobsacB. Similar to plasmid disruption, after being introduced into *G. sulfurreducens* CL-1 strain by the *E.coli* S17 strain, the plasmid can be integrated into the flanking regions of target genes in the chromosome. The colonies were selected by NBAF agar plate with 200 µg/ml kanamycin, and then NBAF agar plates with 10% sucrose were used to select the second recombination. The positive hits were not able to grow on kanamycin agar plates. The complementations were constructed by cloning target genes on plasmid pRK2-Geo2i and conjugated into in-frame deletion mutants. The expression of target proteins was induced by 500 µM vanillate. All *G. sulfurreducens* colonies were grown on an NBAF agar plate with 200 µg/ml kanamycin at 30 °C under dark and strict anaerobic conditions[83]. Gene disruption and in-frame gene deletions were checked by flanking PCR & whole-genome sequencing respectively. Truncations and point mutations were constructed by Q5® Site-Directed Mutagenesis Kit (Cat. No. E0554S, New England Biolabs).

Nanowire purification. Nanowires were purified as described previously[28] with minor modifications. 300 ml of *G. sulfurreducens* cells were collected in 50 ml tubes after five days and spun at 8000 g for 15 min. 30 min after decanting supernatants and removing the remaining liquids, the whole cell weights were measured and used to normalize the loading volume for protein gel later. The pellets were resuspended in 150 mM ethanolamine pH 10.5, added into a Waring Commercial Blender (Cat. No. 7011S), and vortexed at low speed for 2 min. A 30 min-long 13000 g centrifugation was used to remove the bacterial cells. Then, a 1 h-long 23000g centrifugation was used to remove the remaining impurities. Cytochrome filaments were precipitated at another 1 h-long 13000g centrifugation from supernatants after overnight incubation of 12.5% ammonium sulfate at 4 °C. Red pellets are carefully resuspended in 500 µl 150 mM ethanolamine pH 10.5.

Sodium dodecyl sulfate–polyacrylamide gel electrophoresis (SDS-PAGE) and heme staining gels. For SDS-PAGE, after boiling in 1x Laemmli Sample buffer (BioRad, Cat. No 1610747) with 2.5% β-mercaptoethanol for 12 min, the protein samples were run on 4-20% gradient SDS-PAGE gels (Bio-Rad, Cat. No 4568093). The electrophoresis was powered by PowerPac Basic (Bio-Rad) at 190 V for 35 min. For the narrow band split of periplasmic OmcS in Fig. 1D, the setting is 130 min for running time and 150 V for voltage. PageRuler Prestained Protein ladder (Thermo Scientific, product No. #26616) was used to compare the protein molecular weights. The gels were stained in GelCode Blue Safe Protein Stain (Thermo Scientific, REF 1860957) for 1h and destained in deionized water overnight. For heme staining, under dark conditions, 4-20% gradient SDS-PAGE gels were soaked in the mixture of 35 ml 0.5 M sodium acetate (pH 5.0) and 15 ml methanol with 30 mg TMB (3,3,5,5-tetramethylbenzidine) thoroughly dissolved. 300 µl of H_2O_2 was added after ~ 3 min. Heme containing bands turned blue after another 5 min[84,85]. To avoid terminating the color reaction, the reducing reagent β-mercaptoethanol was avoided for heme staining, which accounts for a shift of some protein bands between the heme-staining gels and the Coomassie blue staining gels.

Mass spectrometry for the filament fraction. Protein bands on 4-20% gradient SDS-PAGE gel stained within GelCode Blue Safe Protein Stain (Thermo Scientific, REF 1860957) were carefully incised and sent to Mass Spectrometry & Proteomics Resource at Yale University. Filament fractions were processed through trypsin digestion and liquid chromatography with tandem mass spectrometry (LC-MS/MS). LC-MS/MS analysis was performed on a Thermo Scientific Q Exactive HF-X equipped with a Waters Acquity M-class UPLC system utilizing a binary solvent system (A: 100% water, 0.1% formic acid; B: 100% acetonitrile, 0.1% formic acid). Proteome Discoverer software (version 2.2.0.388, Thermo Scientific) was used to extract tandem mass spectra, and the Mascot algorithm (version 2.6.1, Matrix Science) was used to search in-house against a *G. sulfurreducens* proteome with methionine oxidation and cysteine carbamidomethylation configured as variable modifications. Searches of standard and decoy databases were operated at a 95% confidence level ($p<0.05$). The validation of MS/MS-based peptide and protein identifications was conducted by Scaffold Q+S (version 5.0.1, Proteome Software Inc., Portland, OR). The Scaffold Local FDR algorithm accepted peptide identifications that were established at greater than 95% probability and accepted protein identifications that were established at more than 99% probability and contained at least 2 identified peptides[86,87]. iBAQ (intensity-based absolute quantitation) and emPAI (exponentially modified protein abundance index) are used for quantitative methods.

Negative staining transmission electron microscopy (TEM). CF400-CU grids (Electron Microscopy Sciences) were first plasma cleaned at low power for 40 s, and the samples containing filament proteins or bacteria cells were drop cast on the grids and absorbed to the grids for 5 minutes. Then, the excessive liquid was removed using filter paper. Then, the grids were floated on top of 50 µl droplets of 1% phosphotungstic acid with the carbon side facing the liquid. Then, the excessive stain was removed with filter papers, and the grids were allowed to air dry before checking under TEM. TEM images were taken with a JEM-1400 (JEOL) microscope on Yale West Campus with an 80 kV operating voltage. RELION-3 conducted a two-dimension average of the OscG ring[88]. For the length distribution of OmcS nanowires, the cells with point-mutated OscG (ΔΔmot-1&2) grew in 100 ml NBAF medium with 50 µM vanillate and 200 µg/ml kanamycin, and were examined 4-6 days after the inoculation. To observe the sinusoidal feature of OmcS nanowires, bacterial cells were diluted in MilliQ water to clean the background and examined with an image resolution higher than 0.8 nm/pixel. Only unambiguous cell-attached single OmcS nanowires were included in the analysis. Each *G. sulfurreducens* cell was not heavily aggregated and had clear surroundings.

Atomic force microscopy (AFM) imaging. AFM used soft cantilevers (OMCL-AC240TS-R3, OLYMPUS) whose nominal force constant is 2 N/m and resonance frequency is 70 kHz. Asylum Research software was used to calibrate the tips' free-air amplitude, and the thermal vibration method was used to capture the spring constant. AC-air topography mode was used to image samples with a Cypher ES scanner. For AFM imaging of recombinant OscG, 10 µl of purified OscG protein was drop cast on the mica surface and imaged immediately afterwards. A minimum of 15 individual OscG protein complexes were imaged to estimate their heights using the Gwyddion software[89]. The convolution effect of the AFM tip led to enlarged lateral (X-Y) size compared to the measured OscG height.

Bacterial growth with Fe(III) oxide and MnO_2. Based on NBAF media, a non-chelated mineral mix was utilized, and fumarate (40 mM) was substituted by Fe (III) oxide (~110 mM) as the terminal electron acceptor [90]. The acetate concentration was increased to above 30 mM. Fe (III) was precipitated from a $FeCl_3$ solution and washed 3 times with ddH_2O. Fe (II) was measured through a ferrozine assay[91]. Iron oxide cultures were taken and solubilized in 0.5 M HCl in the dark overnight. Ferrozine was prepared with 1 g/L in 50 mM HEPES. Acid-extracted Fe (II) was diluted in ferrozine for absorbance measurements at 562 nm. Fe (II) standards were prepared from ferrous ethylenediammonium sulfate. For manganese oxide cultures, fumarate (40 mM) in NBAF media was replaced by 100 mM manganese (IV) oxide (SKU 8059581000, Sigma-Aldrich). Filament fractions are difficult to obtain from metal oxide cultures due to low biomass.

Subcellular fractionations. Fractionation of *G. sulfurreducens* cells was performed by using a previously established protocol[22,31] with the following modifications. 1 L of stationary phase culture grown in NBAF was pelleted at 8,000 g for 15 min at 4 °C. After extraction of periplasm fraction, other fractions were extracted from the pellet. We used 0.1 M triethanolamine pH 8, 0.5 M sucrose, and no EDTA for spheroplast buffer. Δ*oscG:poscG-6xHis-tag* cells under induction of 200 µM vanillate were used for Fig.S5A-D, the WT strain was used for Fig.S5E, and the *Ctrl* strain cells were used for Fig.S5F-H.

Immunoblotting and antibody characterization. As described previously[40], for the first antibody, custom polyclonal antibodies were synthesized by LifeTein company (New Jersey) involving the immunization of two rabbits. Each rabbit was immunized with purified proteins or synthetic peptides whose sequences contained the targeted epitopes. Subsequently, the obtained serum was subjected to affinity purification against the respective peptide sequence. For OmpJ, antibodies were raised against purified proteins. For other proteins, the following peptide sequences were used – OscD, KREVAQIDVGDEPC; OscE, NRRQEISDTEGIASSNIIHE; OscF, GRPLNDVTEKAVDDLISK; OscH, EWADKLRKASDVKIFAE; OmcS, KNSGSYQNSNDPTAWG; OmcZ, DSPNAANLGTVKPGLC. The 6xHis-tag was used for the localization of OscG due to a lack of efficient and specific antibodies against OscG. For the secondary antibody, we use Immun-Star AP Goat Anti-Rabbit IgG (H+L) Detection Kit (Cat #1705011, BioRad) by using alkaline phosphatase (AP) conjugated secondary antibody for immunoblots of *G. sulfurreducens.* The antibodies were used at a dilution of 1:3000 for immunoblotting. The first antibodies were typically incubated overnight, and the secondary antibodies were incubated for 30 min. The efficacy of antibodies has been examined on deletion mutants or purified proteins. For filament fractions, loading amounts were normalized by cell weight before purification. For periplasmic fractions and cell lysates from liquid cultures, loading amounts were normalized by the total protein amount measured by the bicinchoninic acid (BCA) assay. For cell lysates from metal oxide cultures, loading amounts were normalized by equal cell culture volume because low biomass does not apply to other normalization methods. For immunoblots of OmcS, the filament fractions were diluted 10 times to avoid oversaturation.

Pull-down of OscH and OscG. 8xHis-Strep II tagged OscH and 6xHis-tagged OscG were expressed from the inducible plasmid pRK2-Geo2i in *G. sulfurreducens* Δ*oscH* and Δ*oscG,* respectively. The *G. sulfurreducens* cultures grew in 10 L jars of NBAF medium at 30 °C under dark environments with the addition of 200 µg/ml kanamycin. Two protein expression conditions were tested: 0 µM and 100 µM inducer vanillate. Cells were harvested after a week of growth, spun down at 8000 g, and

resuspended in the A buffer (50 mM Tris, 50 mM NaCl, pH 8) and the B buffer (150 mM ethanolamine, pH 10.5), respectively. Then, the cells were lysed by ultrasonication, and the soluble fractions were separated from the pellets by 1 h ultracentrifuge at 32000 rpm. The Strep-tagged OscH in the soluble fraction bound to the affinity column (StrepTrap XT, 1 × 5 mL, 29401322, Cytiva company) was eluted by the C buffer (A buffer with 50 mM biotin). The His-tagged OscG bound to the affinity column (HisTrap HP, 1 x 5 ml, 17524801, Cytiva company) was eluted by the D buffer (B buffer with 500 mM imidazole). The elution was characterized by heme stain and immunoblots. The affinity columns were eluted in a linear slope in Fig. 2F & G and Fig. S8A & C. In Fig. S8B, the affinity column was eluted in a linear slope to 60% D buffer (~350 ml elution volume) and then stepped to 100% D buffer.

Proteinase inhibitory assay. 100 ml *G. sulfurreducens* Δ*oscH* cells were supplemented with varying concentrations of cOmplete™, Mini, EDTA-free Protease Inhibitor Cocktail (Cat. No 11836170001, Roche) at exponential stage (OD_{600} = 0.15) and stationary stage (OD_{600} = 0.40) respectively. Cell cultures were collected after 4 days and spun down at 8000 g for 15 min. The pellets were resuspended and lysed by 1ml lysis solution comprised of B-PER Bacterial Protein Extraction Reagent (Cat. No 78248, Thermo Fisher Scientific), 1 mg/ml lysozyme (Cat. No DSL38100-10, DOT Scientific) and 0.1 µl Benzonase nuclease (Cat. No E1014-25ku, Sigma-Aldrich). The supernatants were collected after 16000 g for 15 min and used for immunoblots. Loading volumes were normalized by total protein amounts quantified by BCA assay.

Recombinant protein purification. The recombinant vectors containing the genes encoding OscG protein from *G. sulfurreducens* and OscG homolog from *G. subterraneous*, fused to a Strep-tag, were transformed into *E. coli* BL21 (DE3). The transformed cells were cultured at 37 °C to late exponential phase in 6L LB medium containing 50 µg/ml ampicillin. Protein expression was induced with 0.5 mM isopropyl β-D-1-thiogalactopyranoside (IPTG), and then the cells were harvested by centrifugation at 8000g for 15 min and suspended in 300 ml buffer A (50 mM Tris–HCl pH 8.0, 150 mM NaCl). The suspended cells were sonicated on ice. After ultracentrifugation (100 000g, 1 h at 4 °C), the supernatant was applied onto a 5 ml StrepTrap XT column (Cytiva) equilibrated with buffer A. The column was washed with 200 ml buffer A, and the protein was eluted with a linear gradient of buffer B (A buffer with 50 mM biotin). Afterwards, the elution was further purified with a size exclusion column, Superdex 200 Increase HiScale 16/40 pre-equilibrated with buffer C (50 mM Tris–HCl pH 8.0, 20 mM NaCl). The pEC86 plasmid (CCOS Accession: CCOS 891) with heme maturation apparatus[92] was used for heme-loading in heterologously expressed His-tagged OscD.

Native mass spectrometry. The OscG protein was dialyzed to pH 7.0 200 mM ammonium acetate (RPI, Cat#: A20600-1000.0) buffer for sample preparation. Subsequently, the OscG protein was concentrated above 5 µM for analysis. Q Exactive UHMR (Thermo Fisher Scientific) was equipped with in-house nano-emitter capillaries for native mass spectrometry. These capillaries were prepared by pulling borosilicate glass capillaries (outer diameter 1.5 mm, inner diameter 1.1 mm, length 7.5 cm; Sutter Instruments) using a Flaming/Brown micropipette puller (Model P-1000, Sutter Instruments). The nano-emitters were coated with gold using a rotary-pumped coater Q150R Plus (Quorum Technologies). For the actual measurements, the emitter containing the sample was installed into the Nanospray Flex Ion Source (Thermo Fisher Scientific). Mass spectrometry parameters for protein analysis included a spray voltage of 1.0 kV, a capillary temperature of 300 °C, a resolving power of 6,125 to 12,5000 at m/z of 400, and an ultrahigh vacuum pressure ranging from 4.6 × 10−10 torr to 8.18 × 10−10 torr. In-source trapping was conducted between 100-200V. Analyzed data were visualized in FreeStyle (ThermoFisher) software.

Dynamic light scattering (DLS). DynaPro dynamic light scattering detector (Wyatt Corp., Santa Barbara, CA) was used to collect light scattering data. Dynamics 6 software (Wyatt Corp., Santa Barbara, CA) was applied for data processing. Measurements of Stokes radius were conducted at 300 per second acquisitions at room temperature. The methods of cumulants[93] and regularization[94] were applied to analyze the DLS signals.

Fluorescent spectroscopy. The fluorescence emissions for ATP binding assay were measured by Tecan Infinite M1000 fluorescent plate reader using an excitation wavelength of 403 nm and an emission window of 480 nm to 620 nm. ATP fluorescent analog TNP-ATP triethylammonium salt (TOCRIS Bioscience) increased its fluorescent emission intensity upon binding to proteins. Non-hydrolyzable ATP homolog AMP-PNP (TOCRIS Bioscience) was a competitive inhibitor for TNP-ATP binding to target proteins. The buffer was 50 mM Tris, pH 8.0, 150 mM NaCl, and 2 mM $MgCl_2$. The emission curves were smoothened by moving the average of fluorescent intensities at three consecutive wavelengths.

Protein interactions with OmcS-type nanowires. OmcS nanowires bind to SEC resins in physiologically relevant pH buffers, precluding interaction studies. Therefore, OmcS-type nanowires with ~40% protein sequence identity to OmcS nanowires were purified from *G. subterraneus,* and they did not get stuck in SEC columns under neutral pH buffers. The purified OscG homolog from *G. subterraneus* has ~35% protein sequence identity to OscG purified from *G. sulfurreducens*. Thus, OscG homolog and OmcS-type nanowires from *G. subterraneus* were used for protein interaction studies here. Benzonase (Cat. No E1014-25ku, Sigma-Aldrich) was added during the purification of OscG and OmcS homologs to remove the nucleic acids. Because the amount of purified nanowires were limited, a manually packed SEC column (10 mm inner diameter, 60 cm column length, 47 ml column volume and packed with Sephacryl™ S-200 High Resolution, GE Health) was used for the interaction studies. The elution was insufficient for downstream characterizations. The equilibration buffer is 50 mM Tris, pH 7.4, and 100 mM NaCl. In the protein mixture, the reduction of OscG homolog peak intensities was more significant than the increase of OmcS-type nanowires peak, likely due to some mixed proteins retaining in the entry filter. The column was cleaned with 50 mM NaOH before each interaction experiment to avoid the interference of retained proteins.

AlphaFold predictions and analyses on structural models. Structural models of OscDEFGH were predicted by AlphaFold suite[95]. FoldSeek Server[96] was used to search the structural homologs of the OscH model. The flexible alignments and the calculation of the backbone r.m.s.d for conserved residues of the OscH model were conducted by Fatcat[97]. The docking between the OscH model and the OmcS protomer (PDB: 6ef8)[17] was performed manually. The PyMOL Molecular Graphics System exhibited all visualizations (Version 2.4 Schrödinger, LLC).

QUANTIFICATION AND STATISTICAL ANALYSIS

Unless otherwise stated, quantitative data are expressed in bar and line graphs as mean ± SD (error bar) shown. Unless otherwise stated, differences between two groups were examined using the Student's t-test. Significant P values are indicated (*P<0.05, **P<0.01, and ***P<0.001. Statistical analysis was performed using R (ver. 4.4.1) software.

KEY RESOURCES TABLE

REAGENT or RESOURCE	SOURCE	IDENTIFIER
Antibodies		
Rabbit monospecific antibody anti-OmpJ	This paper	
Rabbit monospecific antibody anti-OscD	This paper	
Rabbit monospecific antibody anti-OscE	This paper	
Rabbit monospecific antibody anti-OscF	This paper	
Rabbit monospecific antibody anti-OscH	This paper	
Rabbit monospecific antibody anti-OmcS	Gu et al. 2021	
Rabbit monospecific antibody anti-OmcZ	Yalcin et al. 2020	
Rabbit monospecific antibody anti-PpcA	This paper	
Rabbit Anti-GroEL Polyclonal Antibody	Abnova	Cat#: PAB5126, RRID: AB_1675789
Anti-His-Tag Rabbit Polyclonal antibody	GeneScript	Cat#: 10500-530
Bacterial and Virus Strains		
E.coli DH5α, MAX Efficiency competent cells	Thermo Scientific	Cat#: 18258012
E.coli S17	R. Simon et al., 1983	
E.coli BL21 (DE3) competent cells	New England Biolabs	Cat#: C2527H
Geobacter sulfurreducens wild-type strains PCA	Coppi et al., 2001	
Geobacter sulfurreducens strain CL-1 (Control)	Leang et al., 2013	
Geobacter sulfurreducens CL1 *omcS, oscD, oscE, oscF, OscG, oscG* deletion mutant strains (designated Δ*omcS,* Δ*oscD,* Δ*oscE,* Δ*oscF,* Δ*oscG,* Δ*oscH* respectively)	This paper	
Geoalkalibacter subterraneus	Greene et al., 2009	DSM 29995
Biological Samples		
N/A		
Chemicals, Peptides, and Recombinant Proteins		
NBAF growth medium	Wang et al., 2019	
Sodium acetate trihydrate	Avantor	Cat#: JTB-3460-05
L-Cysteine hydrochloride monohydrate	Sigma-Aldrich	Cat#: W779989-100G
Lysozyme	Scientific inc.	Cat#: DSL38100-10
Proteinase K	New England Biolabs	Cat#: P8107S
RNAprotect Bacteria Reagent	QIAGEN	Cat#: 1018380
Kanamycin	RPI	Cat#: K22000-25.0
Vanillic acid	TCI	Cat#: V0017
Ethanolamine	RPI	Cat#: E16800-1.0
Ammonium sulfate (saturated solution)	Abcam	Cat#: ab273568
Laemmli Sample buffer	BioRad	Cat#: 1610747
β-mercaptoethanol	Sigma-Aldrich	Cat#: M6250
PageRuler Prestained Protein ladder	Thermo Scientific	Cat#: 26616
GelCode Blue Safe Protein Stain	Thermo Scientific	Cat#: 1860957
TMB (3,3,5,5-tetramethylbenzidine)	Santa Cruz Biotechnology	Cat#: sc-208442B
Hydrogen peroxide	Avantor	Cat#: 5240-05
Phosphotungstic acid, n-Hydrate	Avantor	Cat#: MK282402
Iron (III) Chloride	Beantown Chemical	Cat#: 137640-1kg
Ferrozine (3-(2-Pyridyl)-5,6-diphenyl-1,2,4-triazine-p,p′-disulfonic acid sodium salt)	Sigma-Aldrich	Cat#: P9762-5g
Manganese (IV) oxide	Sigma-Aldrich	Cat#: 8.05958
Biotin	Cayman Chemical	Cat#: 22582
Imidazole	Acros Organics	Cat#: 122020020
cOmplete™, Mini, EDTA-free Protease Inhibitor Cocktail	Roche	Cat#: 11836170001

B-PER Bacterial Protein Extraction Reagent	Thermo Scientific	Cat#: 78248
Benzonase nuclease	Sigma-Aldrich	Cat#: E1014-25ku
Isopropyl β-D-1-thiogalactopyranoside (IPTG)	RPI	Cat#: I56000-25.0
Ampicillin	RPI	Cat#: A40040-25.0
Ammonium acetate	RPI	Cat#: A20600-1000.0
TNP-ATP triethylammonium salt	TOCRIS Bioscience	Cat#: 2464
AMP-PNP	TOCRIS Bioscience	Cat#: 6086
Critical Commercial Assays		
RNeasy Mini Kit	QIAGEN	Cat#: 74104
TURBO DNA-free kit	Invitrogen	Cat#: AM1907
SuperScript First-Strand Synthesis System	Invitrogen	Cat#: 11904018
KAPA SYBR FAST qPCR Kit Master Mix (2X)	Roche	Cat#: KK4605
Q5 Site-Directed Mutagenesis Kit	New England Biolabs	Cat#: E0554S
Pierce BCA (Bicinchoninic acid) Protein Assay Kit	Thermo Scientific	Cat#: 23225
Immun-Star™ Goat Anti-Rabbit (GAR)-AP Detection Kit	BioRad	Cat#: 1705011
Deposited Data		
N/A		
Experimental Models: Cell Lines		
N/A		
Experimental Models: Organisms/Strains		
N/A		
Oligonucleotides		
N/A		
Recombinant DNA		
pk18mobsacB	Chan et al., 2015	
pRK2-Geo2i	Chan et al., 2015	
pEC86	Arslan et al., 1998	CCOS 891
Software and Algorithms		
PSI-BLAST	Altschul et al., 1997	
Mega-X	Kumar S et al., 2018	
iTOL	Letunic et al., 2021	
SignalP 5.0	Almagro et al., 2019	
Proteome Discoverer software version 2.2.0.388	Thermo Fisher Scientific	
Scaffold Q+S version 5.0.1	Proteome Software Inc., OR	
Asylum Research software version 16	Oxford Instruments	
Gwyddion	Nečas et al. 2012	
FreeStyle software	ThermoFisher	
Dynamics 6 software	Wyatt Corp. CA	
AlphaFold	Jumper et al., 2021. Google DeepMind	
Fatcat	Zhanwen Li et al., 2020	
FoldSeek	Michel van Kempen et al., 2024	
Pymol 2.4	Schrödinger, LLC	
Other		
N/A		

Supplementary Figures and Tables

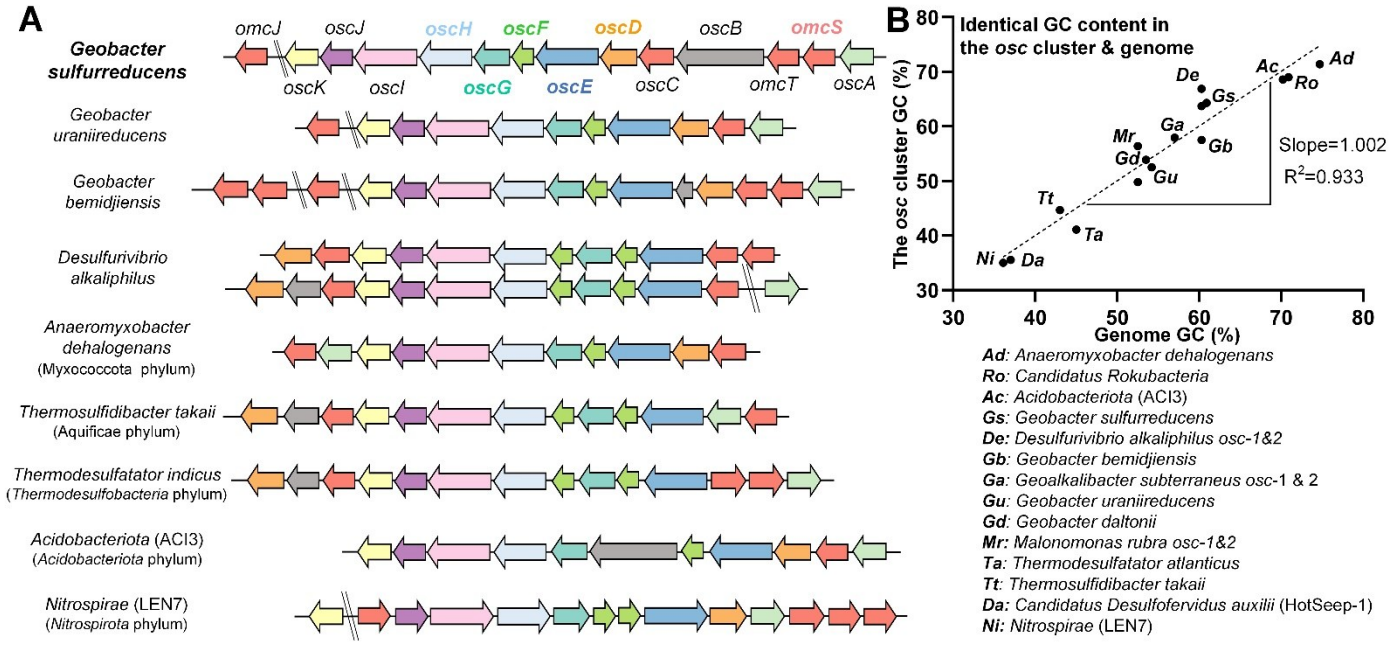

Fig. S1. The *omcS*-companion cluster (*osc*) is widespread and ancient. Genomic organization of the *osc* clusters across several bacterial phyla. Unlabeled species belong to Thermodesulfobacteriota phylum. Homologs are shown in the same color. Non-conserved genes are in grey. **B,** GC% calculated from the *osc* cluster and the corresponding genomes plotted as a correlation curve. The GC contents of the *osc* cluster were almost identical to their genome backgrounds, for species irrespective of high (> 70%) or low (< 40%) GC content.

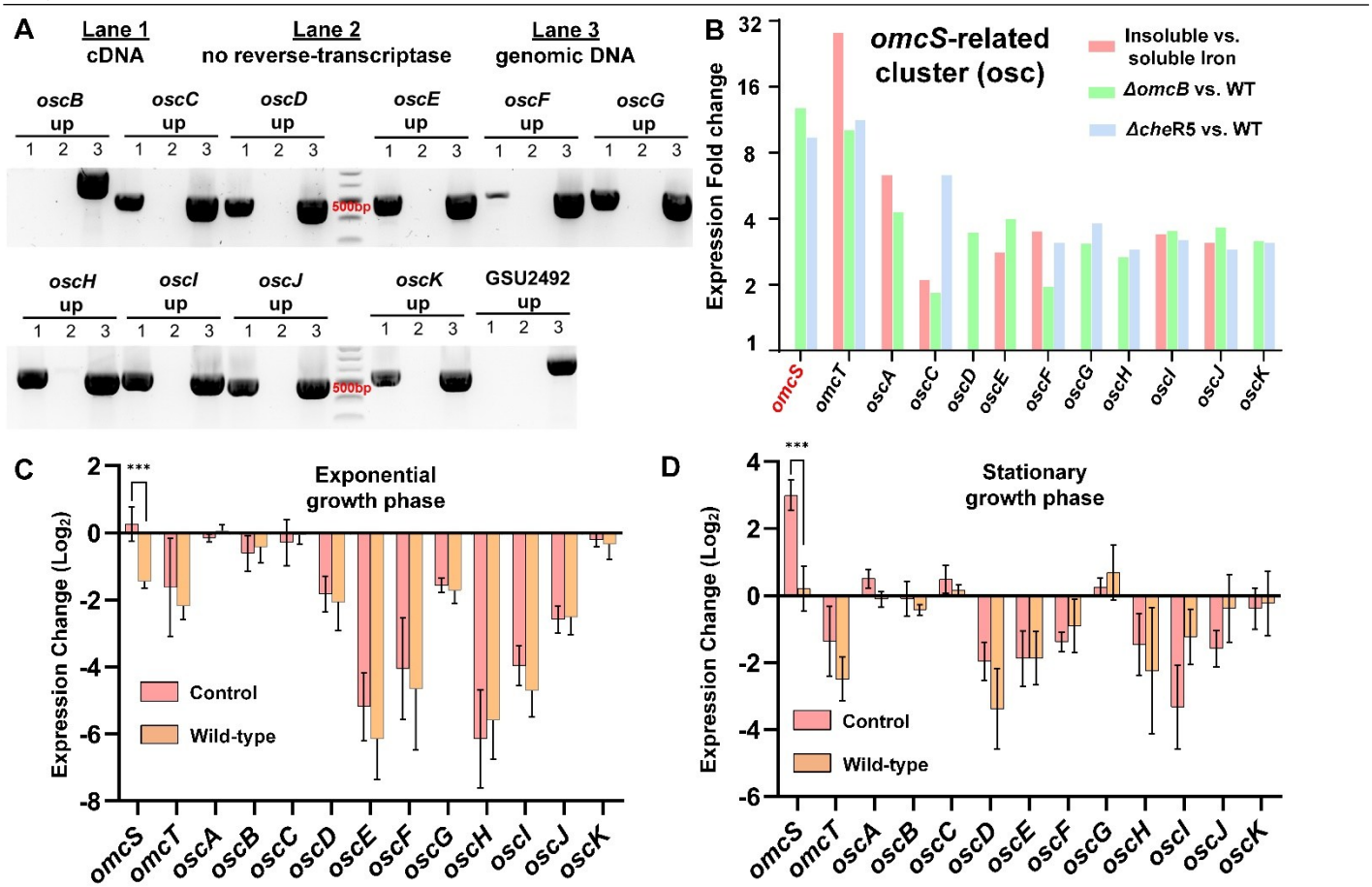

Fig. S2 The *osc* cluster (*oscB-K*) can form an intact operon and is overexpressed with *omcS* during OmcS nanowire formation. A, The agarose gel of qPCR products shows that *oscB* to *oscK* in the *osc* cluster can form an intact operon. All tested regions are the intergenic region between two open reading frames. Only gene names in the 3' end are listed. For example., the intergenic region between *oscB* and *oscC* is denoted as "*oscC* up". Three conditions for each tested region: 1. cDNA; 2. no reverse transcriptase; 3. genomic DNA. DNA marker bands separate by 100bp. The most intense band of the marker lane is 500 bp. **B,** The expression of the *osc* cluster and *omcS* are correlated under various reported growth conditions (see methods for details). **C-D**, The *Ctrl* strain overexpresses *omcS* than WT at **C,** exponential and **D,** stationary phase, while maintain the similar expression level of *osc* genes with WT. Housekeeping gene *rpoD* and *recA* expressions are used as reference for **C,D**. All error bars, SD. n=4 biological replicates, *p<0.05, *** p<0.005.

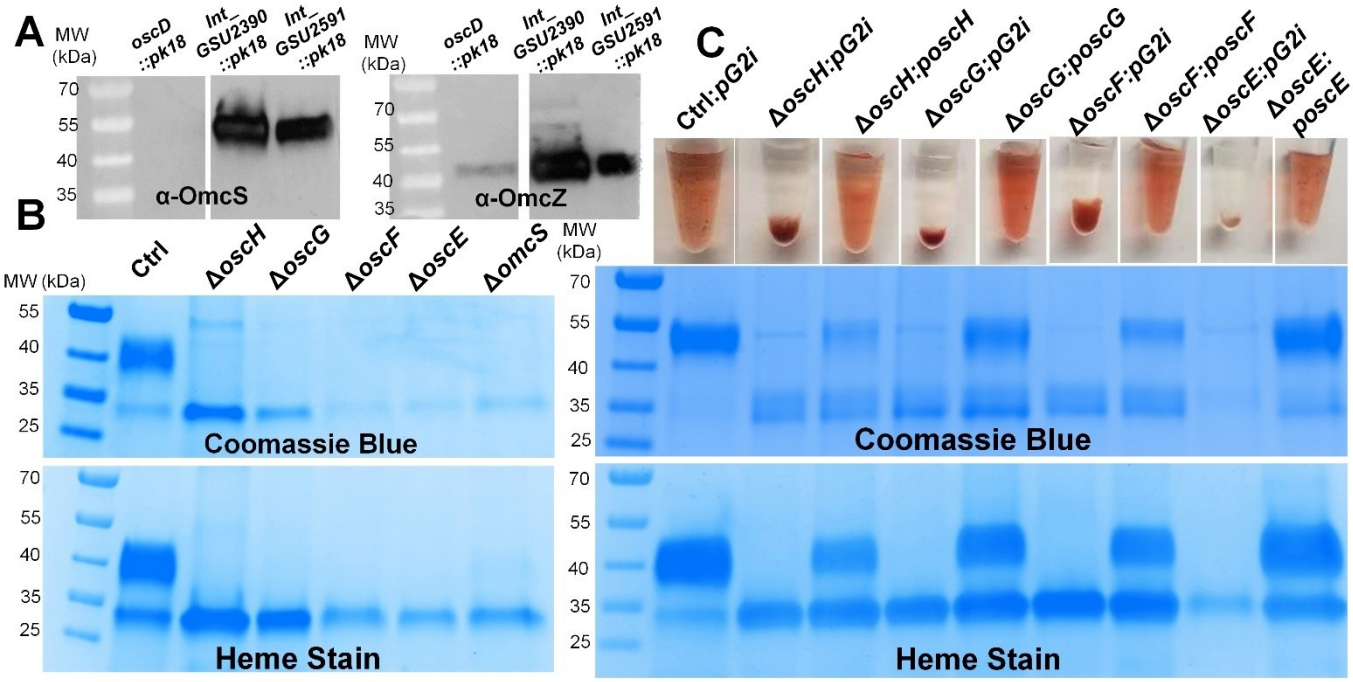

Fig. S3 The *osc* cluster is required for the formation of OmcS nanowires. A, Immunoblots of OmcS and OmcZ in filament fractions from plasmid-disrupted mutants. *oscD*, an *osc* cluster gene. The right two lanes are positive controls using strains with disruption in regions unrelated to the *osc* cluster. Int_GSU2390, intergenic region between GSU2390 and GSU2391. Int_GSU2591, intergenic region between GSU2591 and GSU2592. **B,** Coomassie blue gel and heme staining gel of filament fractions from *Ctrl* and in-frame deletion mutants of *oscEFGH* and *omcS* . **C,** The complementation of deletion mutants Δ*oscH*, Δ*oscG*, Δ*oscF* and Δ*oscE* rescue secretion defects of OmcS nanowires as revealed by solution appearance, Coomassie blue gel and heme staining gel of filament fractions.

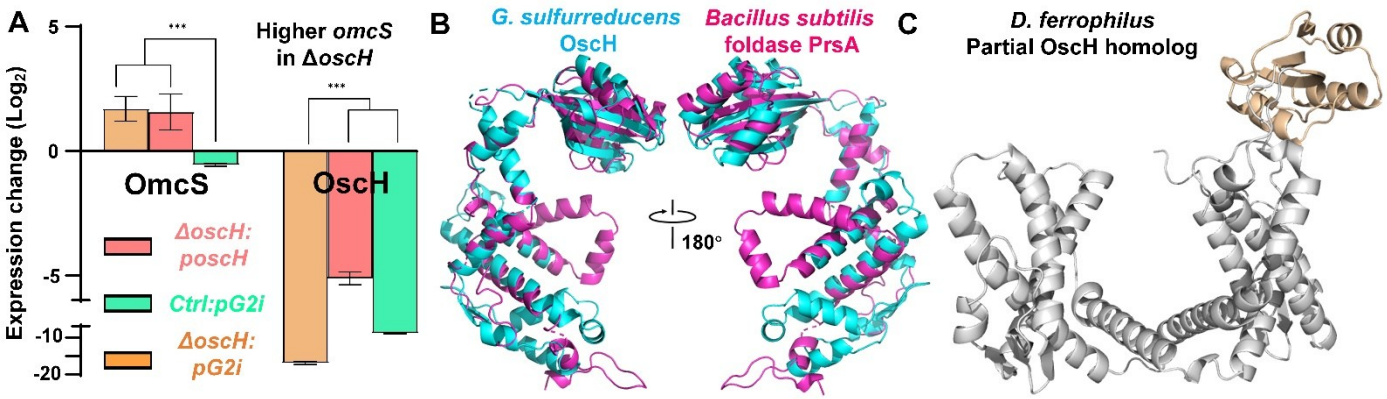

Fig. S4 OscH structure is predicted to be similar to a known isomerase. A, Δ*oscH* showed higher *omcS* expression than the *Ctrl* strain compared to the housekeeping gene *recA*. Error bars, SD. n=4 biological replicates, * p <0.05, *** p<0.005. **B,** Flexible alignment of the PPIase1 half side of the OscH model (cyan) with the foldase PrsA structure (PDB: 4wo7) (purple), having 163 equivalent positions with an RMSD of 2.81Å. **C,** AlphaFold model of OscH from *D. ferrophilus* with confidence score of most residues pLDDT> 90. PPIase domain in orange.

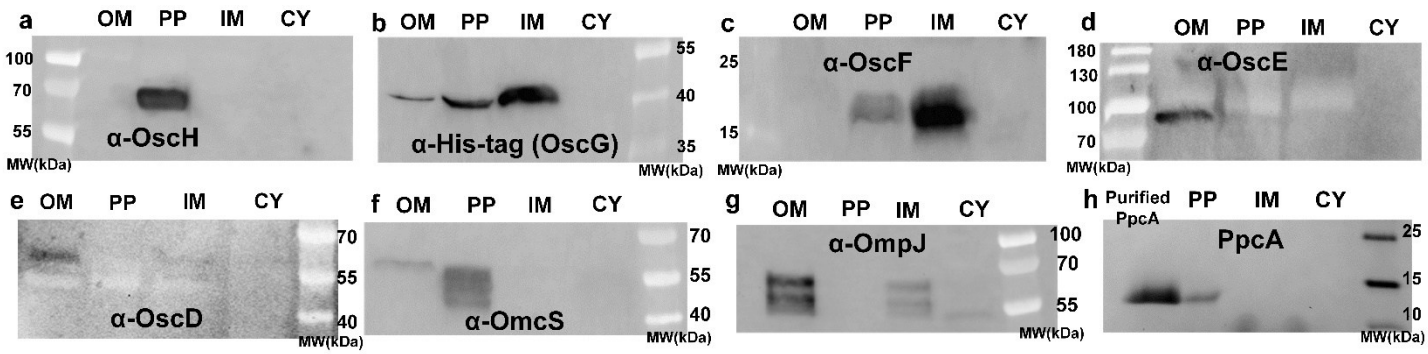

Fig. S5 Subcellular localization of the *osc* cluster proteins OscD-H is consistent with their role in the formation of OmcS nanowires. Immunoblots against **A,** OscH, **B,** His-tagged OscG **C,** OscF, **D,** OscE, **E,** OscD, **F,** OmcS and **G,** outer membrane control: OmpJ, **H,** periplasmic control: Coomassie gel of PpcA. OM, outer membrane; PP, periplasm; IM, inner membrane; CY, cytoplasm. The *oscG* is overexpressed in Δ*oscG:poscG-6xHis-tag* cells under induction of 200 μM vanillate.

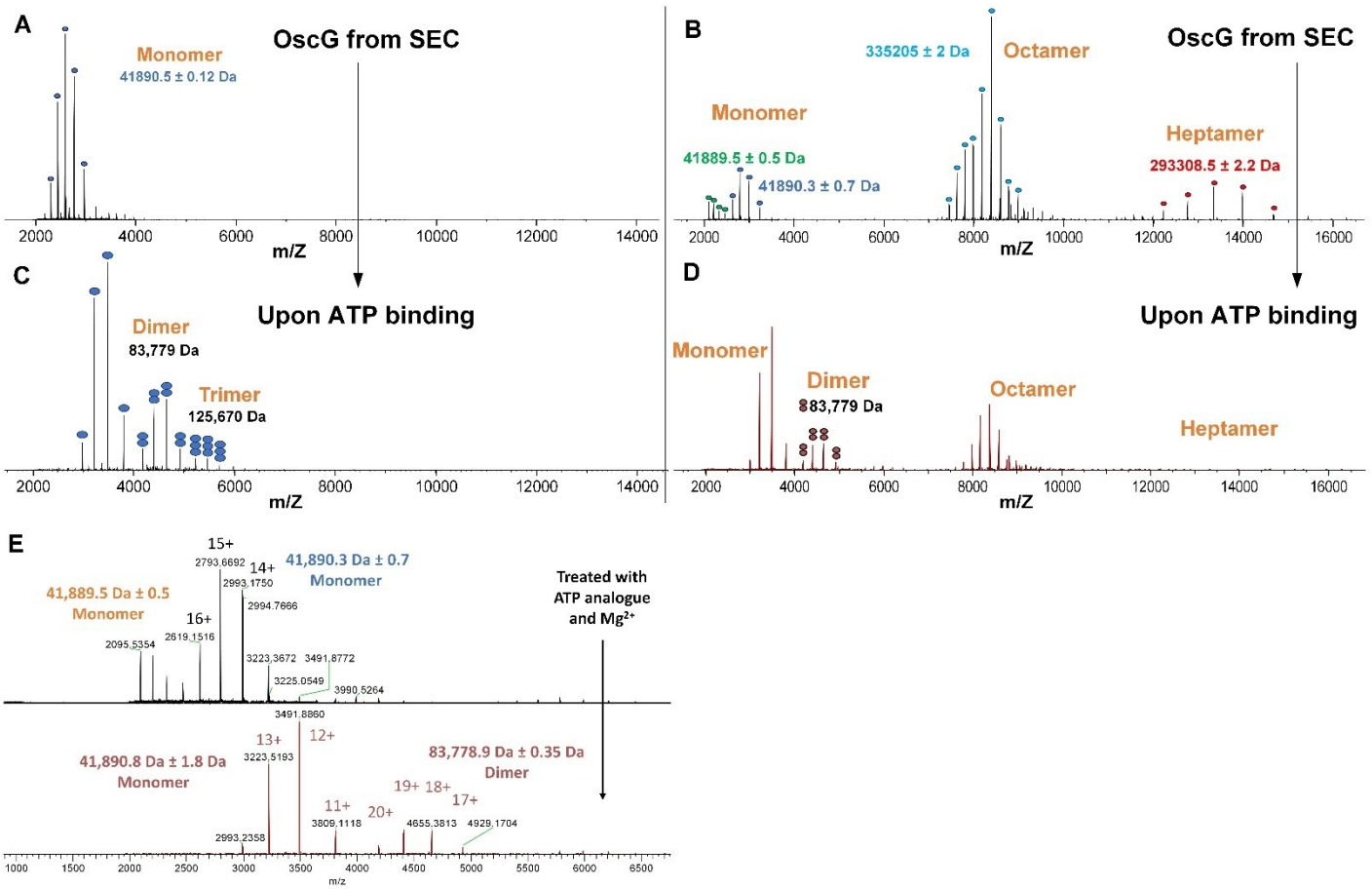

Fig. S6 ATP binding alters the stoichiometry and charge state distributions of OscG subunits. Native mass spectrometry reveals that OscG forms **A,** monomers, **B,** octamers, and heptamers, in ~140 and ~100 ml elution volume from SEC in **Fig. 3A**, respectively. The heptamer is likely from the ionization artefact from octamer. Upon binding to ATP-analog AMP-PNP, OscG oligomerizes into **C-D,** higher stoichiometry. The concentrations of AMP-PNP and $MgCl_2$ are 100 μM and 2 mM in **C** and 50 μM and 1 mM in **D,** respectively. Because native mass spectrometry measurements are not compatible with Mg^{2+} ions, the AMP-PNP treated OscG samples are dialyzed and intensely stirred in 200 mM ammonium acetate pH 7.0 for 2 h before measurements, which washes away AMP-PNP and Mg^{2+} from OscG. Some oligomer status could be less stable during the dialyzing and stirring step. **e** Charge state distributions shift before (top) and after (bottom) the ATP analogue treatment of OscG monomer. The charge states (with "+") and the mass-to-charge ratio (m/z) values are labelled on top of each signal. After the treatment of 50 μM ANP-PNP and 1 mM Mg2+, the monomer population keeps the nearly same molecular weight but have ~3 less charge per monomer and a narrower charge distribution, suggesting a more compact and well-folded conformation.

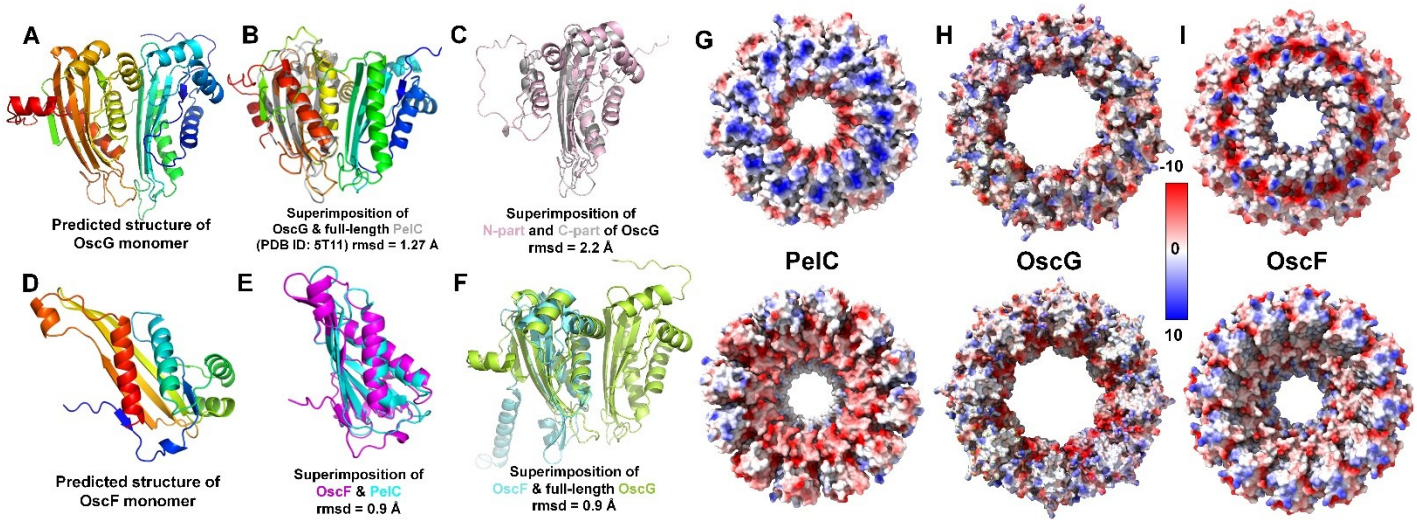

Fig. S7 OscF and OscG structures are predicted to be similar to known secretion channel proteins. AlphaFold model of **A,** OscG and **D,** OscF monomer. **B,** OscG and **E,** OscF monomer models superimposed on the PelC structure (PDB ID: 5T11). PelC forms a polysaccharide secretion channel. **C,** Superimposition of N-part (pink) and C-part (grey) of OscG monomer model. **F**, Superimposition of OscF (cyan) and OscG monomer models (green). **G**, Surface charge distribution of PelC (dodecamer, PDB ID: 5T11) complex shows a negatively charged (red) core, which is predicted to drive the secretion of extracellular polymers. **H-I**, This negatively charged core is absent in **H**, OscG (octamer) and **G**, OscF (dodecamer) complex models predicted by AlphaFold. Top row, top views. Bottom row, bottom views. The redder color represents more negative charge, and the bluer color represents more positive charge.

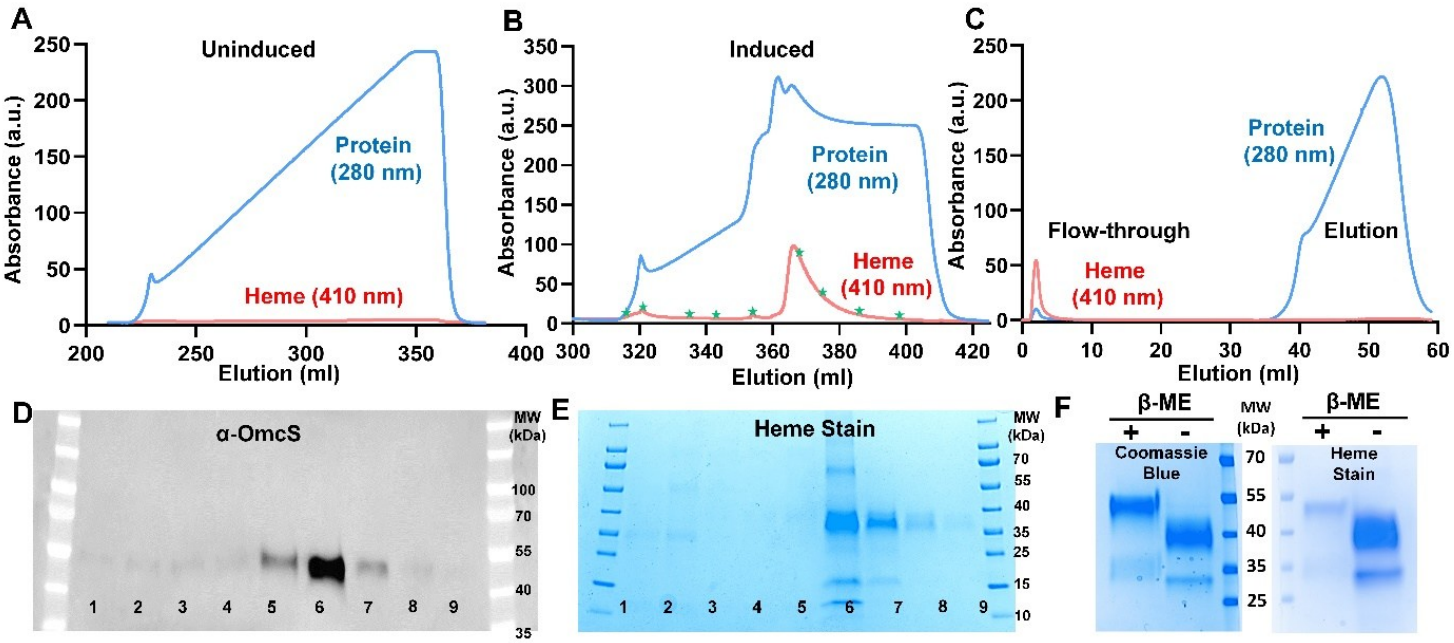

Fig. S8 OmcS is pulled down with OscG *in vivo*. HisTrap affinity purification of His-tagged OscG shows protein (blue) and heme (red) signals in elution fractions from **A,** uninduced and **B,** induced *G. sulfurreducens* cells. Cytochromes can only be pulled down in the induced *G. sulfurreducens* cells. **C,** Purified OmcS nanowires cannot bind to and get eluted from HisTrap affinity column. **D,** Immunoblots and **E,** heme staining confirm that OmcS is enriched in the cytochromes pulled down with OscG suggesting their interactions *in vivo*. Green stars in **B** represent the sampling positions in **D** and **E**. **F**, Reducing reagent β-mercaptoethanol (β-ME) affects the migration positions of OmcS and OmcZ bands. (left) Coomassie blue staining and (right) heme staining of filament fractions from the *Ctrl* strain. After the addition of the reducing reagent β-mercaptoethanol, the OmcS band migrates from ~40kDa position to ~55kDa position, and the intensity of heme staining bands significantly decline. The difference of OmcS band position in **D** vs **E** is due to a lack of a reducing agent β-mercaptoethanol in **E**.

Table S1 The gene annotations for the *osc* cluster. *Molecular weights are calculated from genome including signal peptide, but not cofactors. ** A frameshift is predicted in NCBI gene annotation.

Gene	Gene ID (new)	Gene ID (old)	Amino acids	MW (kDa)*	Annotation
oscK	GS_RS 12525	GSU2493	301	32.37	NHL repeat domain-containing protein
oscJ	GS_RS 12530	GSU2494	426	47.19	16 heme cytochrome**
oscI	GS_RS 12535	GSU2495	646	69.69	26 heme cytochrome
oscH	GS_RS 12540	GSU2496	571	64.64	peptidyl-prolyl cis-trans isomerase
oscG	GS_RS 12545	GSU2497	392	43.43	lipoprotein
oscF	GS_RS 12550	GSU2498	199	21.29	lipoprotein
oscE	GS_RS 12555	GSU2499	725	80.18	hypothetical protein
oscD	GS_RS 12560	GSU3586	482	51.95	β-propeller-containing YVTN family
oscC	GS_RS 12565	GSU2501	437	46.14	Six heme cytochrome, OmcS paralog
oscB	GS_RS 12570	GSU2502	1017	110.54	hypothetical protein
omcT	GS_RS 12575	GSU2503	430	45.53	Six heme cytochrome, OmcS paralog
omcS	GS_RS 12580	GSU2504	432	45.39	Six heme cytochrome, OmcS
oscA	GS_RS 12585	GSU2505	315	33.88	NHL repeat domain-containing protein
omcJ	GS_RS 03500	GSU0701	427	44.36	Six heme cytochrome, OmcS paralog

Table S2. Protein sequence identity of Osc homologs in species other than *G. sulfurreducens*. PSI-blast Osc proteins from *G. sulfurreducens* to homologs from other bacterial genomes. Signal peptides are included. NA, the gene is not found in the target bacteria genome.

Protein Sequence Identity (%)	OmcS	OscA	OscD	OscE	OscF1	OscF2	OscG	OscH	OscI	OscJ	OscK
(1) Thermodesulfobacteriota Phylum											
Geoalkalibacter subterraneus 1st	37.2	33.8	35.7	27.7	50.3	NA	32.0	25.9	47.0	48.0	41.9
Geoalkalibacter subterraneus 2nd	22.2	21.5	19.8	25.8	24.2	21.4	17.2	20.0	32.7	35.1	22.7
Geobacter uraniireducens	52.2	39.5	45.3	39.4	61.7	NA	43.2	37.1	59.3	62.7	47.3
Geobacter bemidjiense	55.3	37.6	40.9	33.1	58.6	NA	39.6	37.0	57.9	58.7	44.9
Candidatus Desulfofervidus auxilii	21.6	22.9	25.3	21.1	31.3	25.3	29.1	23.6	35.0	33.1	24.1
Desulfovibrio ferrophilus	22.4	21.4	19.3	22.6	29.1	23.2	23.5	16.6	36.7	36.0	24.4
Desulfurivibrio alkaliphilus 1st	19.6	NA	19.4	18.9	27.2	21.1	17.1	18.8	33.2	34.2	23.1
Desulfurivibrio alkaliphilus 2nd	24.7	26.1	18.6	16.3	23.4	17.3	20.5	15.6	31.4	31.8	26.3
(2) Other phyla											
Anaeromyxobacter dehalogenans	47.0	38.5	36.2	26.2	58.3	NA	36.5	37.6	49.6	51.4	45.3
Thermosulfidibacter takaii	23.1	26.8	19.3	24.1	33.2	20.8	20.9	16.3	35.9	38.2	18.9
Thermodesulfatator indicus	23.3	23.2	16.8	15.9	31.3	16.0	17.3	20.2	31.3	33.9	19.1
Acidobacteriota ACI3	44.2	40.8	38.9	32.8	62.4	NA	42.6	32.8	48.8	48.2	43.2
Nitrospirae LEN7	21.1	20.8	22.4	18.8	28.3	27.6	20.0	22.6	38.2	32.5	23.4

Table S3. Protein alignment coverage of Osc homologs in species other than *G. sulfurreducens*. PSI-blast Osc proteins from *G. sulfurreducens* to homologs from other bacterial genomes. Signal peptides are included. NA, the gene is not found in the target bacteria genome.

Alignment Coverage (%)	OmcS	OscA	OscD	OscE	OscF	OscG	OscF2	OscH	OscI	OscJ	OscK
(1) Thermodesulfobacteriota Phylum											
Geoalkalibacter subterraneus 1st	99	91	95	99	94	85	NA	92	99	100	98
Geoalkalibacter subterraneus 2nd	92	97	95	76	92	84	94	92	99	91	94
Geobacter uraniireducens	99	95	98	93	87	100	NA	98	100	97	97
Geobacter bemidjiense	99	90	98	86	81	92	NA	99	99	98	94
Candidatus Desulfofervidus auxilii	88	86	98	98	89	82	77	90	99	89	94
Desulfovibrio ferrophilus	80	86	100	88	90	89	87	95	97	96	97
Desulfurivibrio alkaliphilus 1st	89	NA	92	96	84	72	86	90	97	91	87
Desulfurivibrio alkaliphilus 2nd	85	87	95	96	87	90	75	89	97	98	84
(2) Other phyla											
Anaeromyxobacter dehalogenans	87	89	93	97	81	90	NA	98	97	92	98
Thermosulfidibacter takaii	84	86	96	100	93	85	88	89	97	89	97
Thermodesulfatator indicus	83	93	96	88	81	76	93	90	99	91	97
Acidobacteriota ACI3	99	94	92	98	81	81	NA	89	96	100	100
Nitrospirae LEN7	84	97	98	100	94	99	92	90	99	97	87

Table S4. The abundance of important cytochromes detected in filament fractions. A, Mass spectrometry shows that OmcS is the most abundant cytochrome in the filament fraction of *Ctrl* strain with empty vector (*Ctrl:pG2i*). OmcS paralogs are labelled in red. Other known filament-forming cytochromes are labelled in blue. Intensity based absolute quantitation (iBAQ) and exponentially modified protein abundance index (emPAI) are used for quantification. **B**, Peptide coverage of OmcS is over 73%. The identified peptides are highlighted in yellow and the identified modified residues are highlighted in green. The signal peptide sequence which is cleaved in mature OmcS protein is highlighted in light blue.

A

Protein Name	Gene ID	Molecular weight (kDa)	iBAQ	emPAI	Total Spectrum Count
OmcS	GSU2504	45	4.30E+09	63.9	220
OmcZ	GSU2076	49	3.46E+08	0.922	23
OmcT	GSU2503	46	9.81E+07	1.8	16
OmcC	GSU2731	81	6.44E+07	1.92	36
OmcN	GSU2898	292	5.53E+06	0.207	20
ExtA	GSU2645	33	1.75E+07	1.06	8
OmcE	GSU0618	24	4.02E+06	0.238	3
OmcQ	GSU0592	36	2.53E+06	0.81	8
OscC	GSU2501	46	1.35E+06	0.326	5
OmcO	GSU2912	111	8.66E+05	0.151	6
OmcH	GSU2883	91	3.63E+05	0.088	3
OmcJ	GSU0701	44	0	0	0
OmcX	GSU0670	31	0	0	0

B

Table S5. DEAD-type motifs are conserved in OscG homologs among phylogenetically diverse species. Red: acidic residues. Orange: non-acidic residues. Variants show the substitution between glutamate (E) and aspartate (D). Top numbers are residue positions of OscG homologs including signal peptide.

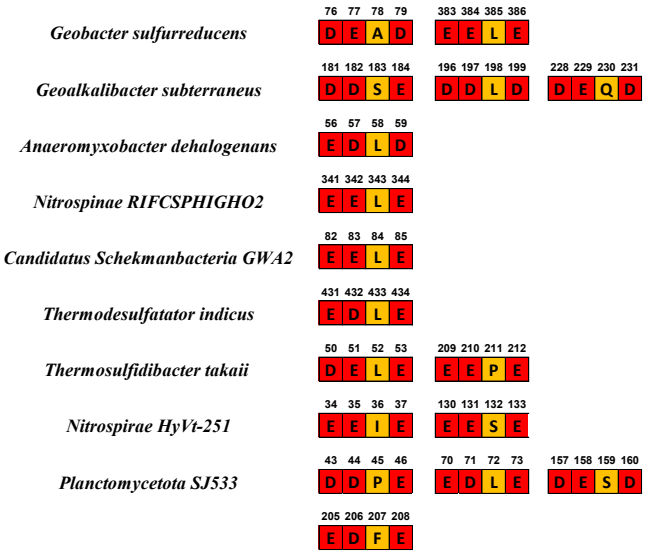

Table S6. List of mutated DEAD-type motifs. OscG from *G. sulfurreducens* has two DEAD-motifs: residue #76-79, DEAD; residue #383-386, EELE. The residue numbers include signal peptides. One or two of the first two acidic amino acids are substituted to alanine in point mutated OscG.

	Point mutant	Substituted amino acid	Mutated DEAD-motifs (mutated residues in red)
1	**ΔΔmot1**	**DE→AA** D76A E77A	AAAD & EELE
2	**ΔΔmot2**	**EE→AA** E383A E384A	DEAD & AALE
3	**Δmot1&2**	**D→A & E→A** D76A & E383A	AEAD & AELE
4	**ΔΔmot1&2**	**DE→AA & EE→AA** D76A &E77A E383A &E384A	AAAD & AALE

Table S7. Primers used for genetic and RT-PCR

(1) For plasmid disruptions	
Name	**Sequence (5'-3')**
oscD_disrupt_F	cgcAAGCTTTATCCTCATCTCCCTCACGCTGG
oscD_disrupt_R	gcgTCTAGACGACACCGAGTTGGACAGGGTAT
G2591_Int_disrupt_F	cgcTCTAGAAGTAACAGTGCGTCTTTGAACGC
G2591_Int_disrupt_R	gcgGGATCCCGGAATCATCAGAGTCAGGAACC
G2390_Int_disrupt_F	cgcTCTAGATAACCGTTGATCGCCGCGTTTTA
G2390_Int_disrupt_R	gcgGGATCCGGCATGGGCGTGAACTAATGGG

(2) For in-frame deletion mutants	
Name	**Sequence (5'-3')**
oscH_3F	cgcaagcttTAGCAGAGTTCGCTCCCCTTC
oscH_3R	TGAAGAAGTCTTTGGTTACGCTGAAGATTTTCGCCGAGTTTTAACGG
oscH_5F	CCGTTAAAACTCGGCGAAAATCTTCAGCGTAACCAAAGACTTCTTCA
oscH_5R	gcgtctagaAAAAGCCGGAAATCCTCTGGATG
oscG_3F	cgcaagcttTGTGCTCGTATTTCAGCTTCTCA
oscG_3R	TGCCGCTGGTTCTGCTCCTCGAACGGATATTGATGAGCCCGTA
oscG_5F	TACGGGCTCATCAATATCCGTTCGAGGAGCAGAACCAGCGGCA
oscG_5R	gcgtctagaGCGTACAATTCATCTGCCAACCA
oscF_3F	cgcaagcttCGATCGCTCTCGTTGAAGAAC
oscF_3R	TATGAGATCACGATTCGTCACCCTCAACGATGTGACTGAGAAAGC
oscF_5F	GCTTTCTCAGTCACATCGTTGAGGGTGACGAATCGTGATCTCATA
oscF_5R	gcgtctagaCGTCTCCTACATCTACAGTGCC
oscE_3F	cgcaagcttCGCTCAGGTCTTCCATGGGGTAG
oscE_3R	CGGATACTCCACGGGTTCATGACCCTGAGATTCGCGTTCTGATT
oscE_5F	AATCAGAACGCGAATCTCAGGGTCATGAACCCGTGGAGTATCCG
oscE_5R	gcgtctagaGACTATTCCCTGACCCGCATC
oscD_3F	cgcaagcttGATGTTGTAGTTGGCGTAGAGGG
oscD_3R	ATTCTCCCAAGCGCATGACGGTGGCGGGCGAAAGGTAAGG
oscD_5F	CCTTACCTTTCGCCCGCCACCGTCATGCGCTTGGGAGAAT
oscD_5R	gcgtctagaCGACCAGGACGGCTCCATTG
omcS_3F	cgcaagcttCTCAGGGACTTGGGCTTGTACC
omcS_3R	ATGGAGGAAATGATGAAAAAGGGGAAGTGCCACGCCAAGGACTAAT
omcS_5F	ATTAGTCCTTGGCGTGGCACTTCCCCTTTTTCATCATTTCCTCCAT
omcS_5R	gcgtctagaCATCAAGCCCATCGAGTTCAAGG

(3) For RT-PCR	
Name	**Sequence (5'-3')**
oscA_up_F	CCCGTGAAGTCCGAGAGGTTATAC
oscA_up_R	GATCCTCTTGCCAAGGCGTG
omcS_up_F	CAGACAGGACGAGCTCTGGGTG
omcS_up_R	GTGTTCGACCGGCAGTTCAAGTT
omcT_up_F	CGGTACTGATGTGGTAGCTGCTG
omcT_up_R	CAACCTGGCATACGAGTTCACGA
oscB_up_F	GAATAGAGGTTGAGCAGGGCGAT
oscB_up_R	CTCAAGGCCCAGACCACGTCAA
oscC_up_F	CTTCTCGTGACAGTTCAGGCAGG
oscC_up_R	CTGACGGTGGTTGATTTCGTGGA
oscD_up_F	AAGGCTCCAGGTAGAGGAACAGT
oscD_up_R	CCTGCTGAGGAATATCGTGACGG
oscE_up_F	GGTTGTAGCGCTGTAGGATCGAG
oscE_up_R	CAAGCGGGTTTACGTGGGGATG
oscF_up_F	GTTGAACACGTCCCTGACCCG
oscF_up_R	GAACAAGGACATGGTCACCACCC
oscG_up_F	GATGCGCTGCTGCTCCATGAAC
oscG_up_R	GGAAGTGGTTAAGCTGGCCAAGA
oscH_up_F	CTCGTGTACCGTTTCAAGGGAGG
oscH_up_R	ACGCTCCAGCAAAATGGTGATCT
oscI_up_F	GGGTTGTGGCAGAGGGTACATTT
oscI_up_R	CGGCTTCACCTATGTCATCCTGG
oscJ_up_F	GGTACACTCCCCCTTCTTCAGGG
oscJ_up_R	GTTCGCCAGCGAGAAGATCCAC
oscK_up_F	CGAGCCGTTCTCGATGCTGTAG
oscK_up_R	TGGACAACATGAAGCGTCAGGAA
GSU2492_up_F	ATAACGACCTGCCGCTCATCTTC
GSU2492_up_R	TCAACATCGGCTGGAAGAACTCG

(4) For qRT-PCR	
Name	**Sequence (5'-3')**
qRT_oscA_F	GAAGGATTCAACCGTGCCGTTC
qRT_oscA_R	CATCGAGCGTAACCGAGGAAGA
qRT_omcS_F	CGTGAACTCGTATGCCAGGTTG
qRT_omcS_R	TCAAGGGTCACGCCAAGATCG
qRT_omcT_F	ATCGGCCACGGTCATGAACTC
qRT_omcT_R	CAAGGCCCAGACCACGTCAA
qRT_oscB_F	GTTCACGTTGACCTCCGGCA
qRT_oscB_R	CCTGCTGAGTTATTTCGTCATGGG
qRT_oscC_F	ACGTAGGGCGTCTTGGTGTTC
qRT_oscC_R	CCAACAACTACACCCTGCTGA
qRT_oscD_F	GCCGGAGATGAAATTGCCCG
qRT_oscD_R	AAGCGGGTTTACGTGGGGATG
qRT_oscE_F	TTTCCATGATAACGCCGAAGGC
qRT_oscE_R	CGAGCTATTCCGGCAACATGAC
qRT_oscF_F	CTGGAGGCTCAGGGAGATAACG
qRT_oscF_R	ACCCCCGAGGAAGTGGTTAAG
qRT_oscG_F	GGTGGCCCAGATCACCATTTTG
qRT_oscG_R	GCCAACAACCTGGAAACCGAT
qRT_oscH_F	GGGAAGGGTCTTGAGGGTGA
qRT_oscH_R	CTTCAATGACCAGAACGCGGC
qRT_oscI_F	CCGAATTGTGGGGCTTGTGG
qRT_oscI_R	CCACAAGGCGAAGCTCAACA
qRT_oscJ_F	TCGTGGCAGTTGAGGCATCC
qRT_oscJ_R	CCCAACAAGGAGAACCTGCTCA
qRT_oscK_F	GGGAACTGGAGATACTCCTTCATCC
qRT_oscK_R	GGGTACCGCTTCATCTCCGA
qRT_recA_F	CACCGGCATAATCTCCAAGT
qRT_recA_R	ATCTTGCGGATATCGAGACG
qRT_rpoD_F	CATCCGCAGAACTTTTTCCTCCC
qRT_rpoD_R	GATTCACACCTGGGGGATTTCATC

References

1. Shi, L., Dong, H., Reguera, G., Beyenal, H., Lu, A., Liu, J., Yu, H.-Q., and Fredrickson, J.K. (2016). Extracellular electron transfer mechanisms between microorganisms and minerals. Nature Reviews Microbiology 14, 651-662. https://doi.org/10.1038/nrmicro.2016.93.
2. Wegener, G., Krukenberg, V., Riedel, D., Tegetmeyer, H.E., and Boetius, A. (2015). Intercellular wiring enables electron transfer between methanotrophic archaea and bacteria. Nature 526, 587-590. https://doi.org/10.1038/nature15733.
3. McGlynn, S.E., Chadwick, G.L., Kempes, C.P., and Orphan, V.J. (2015). Single cell activity reveals direct electron transfer in methanotrophic consortia. Nature 526, 531-535. https://doi.org/10.1038/nature15512.
4. Atkinson, J.T., Su, L., Zhang, X., Bennett, G.N., Silberg, J.J., and Ajo-Franklin, C.M. (2022). Real-time bioelectronic sensing of environmental contaminants. Nature 611, 548-553. https://doi.org/10.1038/s41586-022-05356-y.
5. Light, S.H., Su, L., Rivera-Lugo, R., Cornejo, J.A., Louie, A., Iavarone, A.T., Ajo-Franklin, C.M., and Portnoy, D.A. (2018). A flavin-based extracellular electron transfer mechanism in diverse Gram-positive bacteria. Nature 562, 140-144. https://doi.org/10.1038/s41586-018-0498-z.
6. Saunders, S.H., Edmund, C., Yates, M.D., Otero, F.J., Trammell, S.A., Stemp, E.D., Barton, J.K., Tender, L.M., and Newman, D.K. (2020). Extracellular DNA promotes efficient extracellular electron transfer by pyocyanin in *Pseudomonas aeruginosa* biofilms. Cell 182, 919-932. https://doi.org/10.1016/j.cell.2020.07.006.
7. Edwards, M.J., White, G.F., Butt, J.N., Richardson, D.J., and Clarke, T.A. (2020). The crystal structure of a biological insulated transmembrane molecular wire. Cell 181, 665-673 e610. https://doi.org/10.1016/j.cell.2020.03.032.
8. Levar, C.E., Rollefson, J.B., and Bond, D.R. (2012). Energetic and Molecular Constraints on the Mechanism of Environmental Fe(III) Reduction by Geobacter. In Microbial Metal Respiration: From Geochemistry to Potential Applications, J. Gescher, and A. Kappler, eds. (Springer Berlin Heidelberg), pp. 29-48. https://doi.org/10.1007/978-3-642-32867-1.
9. Lovley, D.R., Ueki, T., Zhang, T., Malvankar, N.S., Shrestha, P.M., Flanagan, K.A., Aklujkar, M., Butler, J.E., Giloteaux, L., Rotaru, A.-E. et al. (2011). *Geobacter*: The microbe electric's physiology, ecology, and practical applications. Advances in Microbial Physiology 59, 1-100. https://doi.org/10.1016/B978-0-12-387661-4.00004-5.
10. Morita, M., Malvankar, N.S., Franks, A.E., Summers, Z.M., Giloteaux, L., Rotaru, A.E., Rotaru, C., and Lovley, D.R. (2011). Potential for direct interspecies electron transfer in methanogenic wastewater digester aggregates. mBio 2, e00159-00111. https://doi.org/10.1128/mBio.00159-11.
11. Shrestha, P.M., Malvankar, N.S., Werner, J.J., Franks, A.E., Elena-Rotaru, A., Shrestha, M., Liu, F., Nevin, K.P., Angenent, L.T., and Lovley, D.R. (2014). Correlation between microbial community and granule conductivity in anaerobic bioreactors for brewery wastewater treatment. Bioresour Technol 174, 306-310. https://doi.org/10.1016/j.biortech.2014.10.004.
12. Malvankar, N.S., Lou, J., Nevin, K., Franks, A.E., Tuominen, M.T., and Lovley, D.R. (2012). Electrical conductivity in a mixed-species biofilm. Applied and Environmental Microbiology 78, 5967-5971. https://doi.org/10.1128/AEM.01803-12.
13. Logan, B.E., Rossi, R., Ragab, A.a., and Saikaly, P.E. (2019). Electroactive microorganisms in bioelectrochemical systems. Nature Reviews Microbiology 17, 307-319. https://doi.org/10.1038/s41579-019-0173-x.
14. Renslow, R.S., Babauta, J.T., Dohnalkova, A.C., Boyanov, M.I., Kemner, K.M., Majors, P.D., Fredrickson, J.K., and Beyenal, H. (2013). Metabolic spatial variability in electrode-respiring Geobacter sulfurreducens biofilms. Energy & Environmental Science 6, 1827-1836. https://doi.org/10.1039/C3EE40203G.
15. Malvankar, N.S., Vargas, M., Nevin, K.P., Franks, A.E., Leang, C., Kim, B.C., Inoue, K., Mester, T., Covalla, S.F., Johnson, J.P. et al. (2011). Tunable metallic-like conductivity in microbial nanowire networks. Nature Nanotechnology 6, 573-579. https://doi.org/10.1038/nnano.2011.119
16. Yalcin, S.E., and Malvankar, N. (2020). The blind men and the filament: Understanding structures and functions of microbial nanowires Current Opinion in Chemical Biology 59, 193-201. https://doi.org/10.1016/j.cbpa.2020.08.004.
17. Wang, F., Gu, Y., O'Brien, J.P., Yi, S.M., Yalcin, S.E., Srikanth, V., Shen, C., Vu, D., Ing, N.L., Hochbaum, A.I. et al. (2019). Structure of microbial nanowires reveals stacked hemes that transport electrons over micrometers. Cell 177, 361-369 e310. https://doi.org/10.1016/j.cell.2019.03.029.
18. Filman, D.J., Marino, S.F., Ward, J.E., Yang, L., Mester, Z., Bullitt, E., Lovley, D.R., and Strauss, M. (2019). Cryo-EM reveals the structural basis of long-range electron transport in a cytochrome-based bacterial nanowire. Communications Biology 2, 219. https://doi.org/10.1038/s42003-019-0448-9
19. Yalcin, S.E., O'Brien, J.P., Gu, Y., Reiss, K., Yi, S.M., Jain, R., Srikanth, V., Dahl, P.J., Huynh, W., Vu, D. et al. (2020). Electric field stimulates production of highly conductive microbial OmcZ nanowires. Nature Chemical Biology 16, 1136-1142. https://doi.org/10.1038/s41589-020-0623-9.
20. Gu, Y., Guberman-Pfeffer, M.J., Srikanth, V., Shen, C., Giska, F., Gupta, K., Londer, Y., Samatey, F.A., Batista, V.S., and Malvankar, N.S. (2023). Structure of *Geobacter* cytochrome OmcZ identifies mechanism of nanowire assembly and conductivity. Nature Microbiology 8, 284-298. https://doi.org/10.1038/s41564-022-01315-5.
21. Wang, F., Chan, C.H., Suciu, V., Mustafa, K., Ammend, M., Si, D., Hochbaum, A.I., Egelman, E.H., and Bond, D.R. (2022). Structure of *Geobacter* OmcZ filaments suggests extracellular cytochrome polymers evolved independently multiple times. eLife 11, e81551. https://doi.org/10.7554/eLife.81551.
22. Gu, Y., Srikanth, V., Salazar-Morales, A.I., Jain, R., O'brien, J.P., Yi, S.M., Soni, R.K., Samatey, F.A., Yalcin, S.E., and Malvankar, N. (2021). Structure of *Geobacter* pili reveals secretory rather than nanowire behavior. Nature 597, 430-434 https://doi.org/10.1038/s41586-021-03857-w
23. Wang, F., Mustafa, K., Suciu, V., Joshi, K., Chan, C.H., Choi, S., Su, Z., Si, D., Hochbaum, A.I., Egelman, E.H. et al. (2022). Cryo-EM structure of an extracellular *Geobacter* OmcE cytochrome filament reveals tetrahaem packing. Nature Microbiology 7, 1291-1300. https://doi.org/10.1038/s41564-022-01159-z.
24. Lovley, D.R. (2022). On the existence of pilin-based microbial nanowires. Frontiers in Microbiology 13. https://doi.org/10.3389/fmicb.2022.872610.
25. Lovley, D.R. (2023). Response to Wang et al.: evidence contradicting the cytochrome-only model. Trends in Microbiology. https://doi.org/10.1016/j.tim.2023.03.006.
26. Wang, F., Craig, L., Liu, X., Rensing, C., and Egelman, E.H. (2023). Microbial nanowires: type IV pili or cytochrome filaments? Trends in Microbiology 31, 384-392. https://doi.org/10.1016/j.tim.2022.11.004.
27. Yalcin, S.E., and Malvankar, N.S. (2021). Seeing is believing: Novel imaging methods help identify structure and function of *Geobacter* nanowires in electricity-producing biofilms in Roadmap on emerging concepts in the physical biology of bacterial biofilms: from surface sensing to community formation Physical Biology 18, 32-25. https://doi.org/10.1088/1478-3975/abdc0e
28. Neu, J., Shipps, C., Guberman-Pfeffer, M., Shen, C., Vishok, S., Spies, J.A., Kirchhofer, N.D., Yalcin, S.E., Brudvig, G.W., Batista, V.S. et al. (2022). Microbial biofilms as living photoconductors due to ultrafast electron transfer in cytochrome OmcS nanowires. Nature Communications 13, 1-12. https://doi.org/10.1038/s41467-022-32659-5.
29. Dahl, P.J., Yi, S.M., Gu, Y., Acharya, A., Shipps, C., Neu, J., O'Brien, J.P., Morzan, U.N., Chaudhuri, S., Guberman-Pfeffer, M.J. et al. (2022). A 300-fold conductivity increase in microbial cytochrome nanowires due to temperature-induced restructuring of hydrogen bonding networks. Science Advances 8, eabm7193. https://doi.org/10.1126/sciadv.abm7193.
30. Summers, Z.M., Fogarty, H.E., Leang, C., Franks, A.E., Malvankar, N.S., and Lovley, D.R. (2010). Direct exchange of electrons within aggregates of an evolved syntrophic coculture of anaerobic bacteria. Science 330, 1413-1415. https://doi.org/10.1126/science.1196526.
31. Liu, X., Zhuo, S., Rensing, C., and Zhou, S. (2018). Syntrophic growth with direct interspecies electron transfer between pili-free *Geobacter* species. The ISME Journal 12, 2142–2151. https://doi.org/10.1038/s41396-018-0193-y.
32. Mehta, T., Coppi, M.V., Childers, S.E., and Lovley, D.R. (2005). Outer membrane *c*-type cytochromes required for Fe (III) and Mn (IV) oxide reduction in *Geobacter sulfurreducens*. Applied and Environmental Microbiology 71, 8634-8641. https://doi.org/10.1128/aem.71.12.8634-8641.2005.

33. Yun, J., Malvankar, N.S., Ueki, T., and Lovley, D.R. (2016). Functional environmental proteomics: elucidating the role of a *c*-type cytochrome abundant during uranium bioremediation. The ISME Journal 10, 310-320. https://doi.org/10.1038/ismej.2015.113.
34. Holmes, D.E., Chaudhuri, S.K., Nevin, K.P., Mehta, T., Methe, B.A., Liu, A., Ward, J.E., Woodard, T.L., Webster, J., and Lovley, D.R. (2006). Microarray and genetic analysis of electron transfer to electrodes in *Geobacter sulfurreducens*. Environmental Microbiology 8, 1805-1815. https://doi.org/10.1111/j.1462-2920.2006.01065.x.
35. Jiang, J., He, P., Luo, Y., Peng, Z., Jiang, Y., Hu, Y., Qi, L., Dong, X., Dong, Y., and Shi, L. (2023). The varied roles of pilA-N, omcE, omcS, omcT, and omcZ in extracellular electron transfer by Geobacter sulfurreducens. Frontiers in Microbiology 14. https://doi.org/10.3389/fmicb.2023.1251346.
36. Richter, H., Nevin, K.P., Jia, H., Lowy, D.A., Lovley, D.R., and Tender, L.M. (2009). Cyclic voltammetry of biofilms of wild type and mutant *Geobacter sulfurreducens* on fuel cell anodes indicates possible roles of OmcB, OmcZ, type IV pili, and protons in extracellular electron transfer. Energy & Environmental Science 2, 506-516. https://doi.org/10.1039/B816647A.
37. Zhang, B., Cheng, H.-Y., and Wang, A. (2021). Extracellular electron transfer through visible light induced excited-state outer membrane *c*-type cytochromes of *Geobacter sulfurreducens*. Bioelectrochemistry 138, 107683. https://doi.org/10.1016/j.bioelechem.2020.107683.
38. Li, D.-B., Cheng, Y.-Y., Li, L.-L., Li, W.-W., Huang, Y.-X., Pei, D.-N., Tong, Z.-H., Mu, Y., and Yu, H.-Q. (2014). Light-driven microbial dissimilatory electron transfer to hematite. Physical Chemistry Chemical Physics 16, 23003-23011. https://doi.org/10.1039/C4CP04065A.
39. Meng, H., Zhang, W., Zhu, H., Yang, F., Zhang, Y., Zhou, J., and Li, Y. (2021). Over-expression of an electron transport protein OmcS provides sufficient NADH for d-lactate production in cyanobacterium. Biotechnology for Biofuels 14, 109. https://doi.org/10.1186/s13068-021-01956-4.
40. Dong, F., Lee, Y.S., Gaffney, E.M., Liou, W., and Minteer, S.D. (2021). Engineering *Cyanobacterium* with transmembrane electron transfer ability for bioelectrochemical nitrogen fixation. ACS Catalysis 11, 13169-13179. https://doi.org/10.1021/acscatal.1c03038.
41. Lin, T., Ding, W., Zhang, D., You, Z., Yang, Y., Li, F., Xu, D., Lovley, D.R., and Song, H. (2024). Expression of filaments of the *Geobacter* extracellular cytochrome OmcS in *Shewanella oneidensis*. Biotechnology and Bioengineering 121, 2002-2012. https://doi.org/https://doi.org/10.1002/bit.28702.
42. Lin, T., Ding, W., Zhang, D., You, Z., Yang, Y., Li, F., Xu, D., Lovley, D.R., and Song, H. (2024). Correction to “Expression of filaments of the *Geobacter* extracellular cytochrome OmcS in *Shewanella oneidensis*”. Biotechnology and Bioengineering 121, 2002-2012. https://doi.org/https://doi.org/10.1002/bit.28815.
43. Butler, J.E., Young, N.D., and Lovley, D.R. (2010). Evolution of electron transfer out of the cell: comparative genomics of six *Geobacter* genomes. BMC Genomics 11, 40. https://doi.org/10.1186/1471-2164-11-40.
44. Greene, A.C., Patel, B.K., and Yacob, S. (2009). *Geoalkalibacter subterraneus* sp. nov., an anaerobic Fe (III)-and Mn (IV)-reducing bacterium from a petroleum reservoir, and emended descriptions of the family *Desulfuromonadaceae* and the genus *Geoalkalibacter*. International Journal of Systematic and Evolutionary Microbiology 59, 781-785. https://doi.org/10.1099/ijs.0.001537-0.
45. Wu, Q., Sanford, R.A., and Löffler, F.E. (2006). Uranium (VI) reduction by *Anaeromyxobacter dehalogenans* strain 2CP-C. Applied and Environmental Microbiology 72, 3608-3614. https://doi.org/10.1128/AEM.72.5.3608-3614.2006.
46. Leang, C., Malvankar, N.S., Franks, A.E., Nevin, K.P., and Lovley, D.R. (2013). Engineering *Geobacter sulfurreducens* to produce a highly cohesive conductive matrix with enhanced capacity for current production. Energy & Environmental Science 6, 1901-1908. https://doi.org/10.1039/c3ee40441b.
47. Mitchell, A.M., and Silhavy, T.J. (2019). Envelope stress responses: balancing damage repair and toxicity. Nature Reviews Microbiology 17, 417-428. https://doi.org/10.1038/s41579-019-0199-0.
48. Jakob, R.P., Koch, J.R., Burmann, B.M., Schmidpeter, P.A., Hunkeler, M., Hiller, S., Schmid, F.X., and Maier, T. (2015). Dimeric structure of the bacterial extracellular foldase PrsA. Journal of Biological Chemistry 290, 3278-3292. https://doi.org/10.1074/jbc.M114.622910.
49. Chan, C.H., Levar, C.E., Jiménez-Otero, F., and Bond, D.R. (2017). Genome scale mutational analysis of *Geobacter sulfurreducens* reveals distinct molecular mechanisms for respiration and sensing of poised electrodes versus Fe (III) oxides. Journal of Bacteriology 199, e00340-00317. https://doi.org/10.1128/jb.00340-17.
50. Deng, X., Dohmae, N., Nealson, K.H., Hashimoto, K., and Okamoto, A. (2018). Multi-heme cytochromes provide a pathway for survival in energy-limited environments. Science Advances 4, eaao5682. https://doi.org/doi:10.1126/sciadv.aao5682.
51. Deng, X., and Okamoto, A. (2023). Direct extracellular electron transfer to an indium tin doped oxide electrode via heme redox reactions in *Desulfovibrio ferrophilus* IS5. Electrochimica Acta 453, 142293. https://doi.org/https://doi.org/10.1016/j.electacta.2023.142293.
52. Marmont, L.S., Rich, J.D., Whitney, J.C., Whitfield, G.B., Almblad, H., Robinson, H., Parsek, M.R., Harrison, J.J., and Howell, P.L. (2017). Oligomeric lipoprotein PelC guides Pel polysaccharide export across the outer membrane of *Pseudomonas aeruginosa*. Proceedings of the National Academy of Sciences 114, 2892-2897.
53. Linder, P., and Jankowsky, E. (2011). From unwinding to clamping — the DEAD box RNA helicase family. Nature Reviews Molecular Cell Biology 12, 505-516. https://doi.org/10.1038/nrm3154.
54. Woodbury, D.J., Whitt, E.C., and Coffman, R.E. (2021). A review of TNP-ATP in protein binding studies: benefits and pitfalls. Biophysical Reports 1.
55. Li, J., Santambrogio, C., Brocca, S., Rossetti, G., Carloni, P., and Grandori, R. (2016). Conformational effects in protein electrospray-ionization mass spectrometry. Mass Spectrometry Reviews 35, 111-122. https://doi.org/https://doi.org/10.1002/mas.21465.
56. Pause, A., and Sonenberg, N. (1992). Mutational analysis of a DEAD box RNA helicase: the mammalian translation initiation factor eIF-4A. The EMBO Journal 11, 2643-2654. https://doi.org/https://doi.org/10.1002/j.1460-2075.1992.tb05330.x.
57. Qi, Z., Hamza, I., and O’Brian, M.R. (1999). Heme is an effector molecule for iron-dependent degradation of the bacterial iron response regulator (Irr) protein. Proceedings of the National Academy of Sciences 96, 13056-13061. https://doi.org/doi:10.1073/pnas.96.23.13056.
58. Zenke-Kawasaki, Y., Dohi, Y., Katoh, Y., Ikura, T., Ikura, M., Asahara, T., Tokunaga, F., Iwai, K., and Igarashi, K. (2007). Heme Induces Ubiquitination and Degradation of the Transcription Factor Bach1. Molecular and Cellular Biology 27, 6962-6971. https://doi.org/10.1128/MCB.02415-06.
59. Anantharaman, K., Hausmann, B., Jungbluth, S.P., Kantor, R.S., Lavy, A., Warren, L.A., Rappé, M.S., Pester, M., Loy, A., and Thomas, B.C. (2018). Expanded diversity of microbial groups that shape the dissimilatory sulfur cycle. The ISME Journal 12, 1715-1728. https://doi.org/10.1038/s41396-018-0078-0.
60. Anantharaman, K., Brown, C.T., Hug, L.A., Sharon, I., Castelle, C.J., Probst, A.J., Thomas, B.C., Singh, A., Wilkins, M.J., and Karaoz, U. (2016). Thousands of microbial genomes shed light on interconnected biogeochemical processes in an aquifer system. Nature communications 7, 1-11.
61. Nunoura, T., Oida, H., Miyazaki, M., and Suzuki, Y. (2008). Thermosulfidibacter takaii gen. nov., sp. nov., a thermophilic, hydrogen-oxidizing, sulfur-reducing chemolithoautotroph isolated from a deep-sea hydrothermal field in the Southern Okinawa Trough. International Journal of Systematic and Evolutionary Microbiology 58, 659-665. https://doi.org/https://doi.org/10.1099/ijs.0.65349-0.
62. Alain, K., Postec, A., Grinsard, E., Lesongeur, F., Prieur, D., and Godfroy, A. (2010). Thermodesulfatator atlanticus sp. nov., a thermophilic, chemolithoautotrophic, sulfate-reducing bacterium isolated from a Mid-Atlantic Ridge hydrothermal vent. International Journal of Systematic and Evolutionary Microbiology 60, 33-38. https://doi.org/10.1099/ijs.0.009449-0.
63. Weiss, M.C., Sousa, F.L., Mrnjavac, N., Neukirchen, S., Roettger, M., Nelson-Sathi, S., and Martin, W.F. (2016). The physiology and habitat of the last universal common ancestor. Nature Microbiology 1, 16116. https://doi.org/10.1038/nmicrobiol.2016.116.
64. Vargas, M., Kashefi, K., Blunt-Harris, E.L., and Lovley, D.R. (1998). Microbiological evidence for Fe(III) reduction on early Earth. Nature 395, 65-67. https://doi.org/10.1038/25720.
65. Erwin, J., Shen, C., Saldivar, V., Salazar-Morales, A., Samatey, F., Dahl, P.J., Gu, Y., Yalcin, S., and Malvankar, N. (2024). A widespread porin-cytochrome complex Om(abc)B kickstarts microbial respiration and nanowire formation. Preprint. https://doi.org/10.21203/rs.3.rs-5369439/v1.

66. Rollefson, J.B., Levar, C.E., and Bond, D.R. (2009). Identification of genes involved in biofilm formation and respiration via mini-Himar transposon mutagenesis of *Geobacter sulfurreducens*. Journal of Bacteriology 191, 4207-4217. https://doi.org/10.1128/jb.00057-09.
67. Hernández-Eligio, A., Huerta-Miranda, G.A., Martínez-Bahena, S., Castrejón-López, D., Miranda-Hernández, M., and Juárez, K. (2022). GSU1771 regulates extracellular electron transfer and electroactive biofilm formation in Geobacter sulfurreducens: Genetic and electrochemical characterization. Bioelectrochemistry 145, 108101. https://doi.org/10.1016/j.bioelechem.2022.108101.
68. Murali, R., Yu, H., Speth, D.R., Wu, F., Metcalfe, K.S., Crémière, A., Laso-Pèrez, R., Malmstrom, R.R., Goudeau, D., Woyke, T. et al. (2023). Physiological potential and evolutionary trajectories of syntrophic sulfate-reducing bacterial partners of anaerobic methanotrophic archaea. PLOS Biology 21, e3002292. https://doi.org/10.1371/journal.pbio.3002292.
69. Krukenberg, V., Riedel, D., Gruber-Vodicka, H.R., Buttigieg, P.L., Tegetmeyer, H.E., Boetius, A., and Wegener, G. (2018). Gene expression and ultrastructure of meso-and thermophilic methanotrophic consortia. Environmental microbiology 20, 1651-1666. https://doi.org/10.1111/1462-2920.14077.
70. Sekar, N., Jain, R., Yan, Y., and Ramasamy, R.P. (2016). Enhanced photo-bioelectrochemical energy conversion by genetically engineered cyanobacteria. Biotechnology and Bioengineering 113, 675-679. https://doi.org/https://doi.org/10.1002/bit.25829.
71. Guberman-Pfeffer, M.J., Dorval Courchesne, N.-M., and Lovley, D.R. (2024). Microbial nanowires for sustainable electronics. Nature Reviews Bioengineering. https://doi.org/10.1038/s44222-024-00204-2.
72. Dahl, P.J., Neu, J., Gu, Y., Shipps, C., Batista, V.S., and Malvankar, N.S. (2024). Ultrahigh-mobility microbial cytochrome nanowires generate power from humidity. Preprint. https://doi.org/10.21203/rs.3.rs-4724466/v1.
73. Altschul, S.F., Madden, T.L., Schäffer, A.A., Zhang, J., Zhang, Z., Miller, W., and Lipman, D.J. (1997). Gapped BLAST and PSI-BLAST: a new generation of protein database search programs. Nucleic acids research 25, 3389-3402.
74. Kumar, S., Stecher, G., Li, M., Knyaz, C., and Tamura, K. (2018). MEGA X: molecular evolutionary genetics analysis across computing platforms. Molecular Biology and Evolution 35, 1547.
75. Letunic, I., and Bork, P. (2021). Interactive Tree Of Life (iTOL) v5: an online tool for phylogenetic tree display and annotation. Nucleic Acids Research 49, W293-W296. https://doi.org/10.1093/nar/gkab301.
76. Aklujkar, M., Coppi, M.V., Leang, C., Kim, B.C., Chavan, M., Perpetua, L., Giloteaux, L., Liu, A., and Holmes, D. (2013). Proteins involved in electron transfer to Fe (III) and Mn (IV) oxides by *Geobacter sulfurreducens* and *Geobacter uraniireducens*. Microbiology 159, 515-535.
77. Leang, C., Adams, L.A., Chin, K.-J., Nevin, K.P., Methe, B., Webster, J., Sharma, M., and Lovley, D. (2005). Adaptation to disruption of the electron transfer pathway for Fe (III) reduction in *Geobacter sulfurreducens*. Journal of bacteriology 187, 5918-5926.
78. Tran, H.T. (2009). Investigation of chemotaxis genes and their functions in *Geobacter* species. (University of Massachusetts Amherst).
79. Almagro Armenteros, J.J., Tsirigos, K.D., Sønderby, C.K., Petersen, T.N., Winther, O., Brunak, S., von Heijne, G., and Nielsen, H. (2019). SignalP 5.0 improves signal peptide predictions using deep neural networks. Nature biotechnology 37, 420-423.
80. Alexeyev, M.F. (1999). The pKNOCK series of broad-host-range mobilizable suicide vectors for gene knockout and targeted DNA insertion into the chromosome of gram-negative bacteria. Biotechniques 26, 824-826, 828. https://doi.org/10.2144/99265bm05.
81. Chan, C.H., Levar, C.E., Zacharoff, L., Badalamenti, J.P., and Bond, D.R. (2015). Scarless genome editing and stable inducible expression vectors for *Geobacter sulfurreducens*. Appl. Environ. Microbiol. 81, 7178-7186.
82. Simon, R., Priefer, U., and Pühler, A. (1983). A broad host range mobilization system for in vivo genetic engineering: transposon mutagenesis in gram negative bacteria. Bio/technology 1, 784-791.
83. Coppi, M.V., Leang, C., Sandler, S.J., and Lovley, D.R. (2001). Development of a genetic system for *Geobacter sulfurreducens*. Applied and Environmental Microbiology 67, 3180-3187. https://doi.org/10.1128/aem.67.7.3180-3187.2001.
84. Thomas, P.E., Ryan, D., and Levin, W. (1976). An improved staining procedure for the detection of the peroxidase activity of cytochrome P-450 on sodium dodecyl sulfate polyacrylamide gels. Analytical biochemistry 75, 168-176.
85. Francis Jr, R.T., and Becker, R.R. (1984). Specific indication of hemoproteins in polyacrylamide gels using a double-staining process. Analytical biochemistry 136, 509-514.
86. Shevchenko, A., Tomas, H., Havli, J., Olsen, J.V., and Mann, M. (2006). In-gel digestion for mass spectrometric characterization of proteins and proteomes. Nature protocols 1, 2856-2860.
87. Cox, J., and Mann, M. (2008). MaxQuant enables high peptide identification rates, individualized ppb-range mass accuracies and proteome-wide protein quantification. Nature biotechnology 26, 1367-1372.
88. Zivanov, J., Nakane, T., Forsberg, B.O., Kimanius, D., Hagen, W.J., Lindahl, E., and Scheres, S.H. (2018). New tools for automated high-resolution cryo-EM structure determination in RELION-3. Elife 7. https://doi.org/10.7554/eLife.42166.
89. Nečas, D., and Klapetek, P. (2012). Gwyddion: an open-source software for SPM data analysis. Open Physics 10, 181-188.
90. Lovley, D.R., Stolz, J.F., Nord, G.L., and Phillips, E.J. (1987). Anaerobic production of magnetite by a dissimilatory iron-reducing microorganism. Nature 330, 252-254.
91. Aklujkar, M., Coppi, M.V., Leang, C., Kim, B.C., Chavan, M.A., Perpetua, L.A., Giloteaux, L., Liu, A., and Holmes, D.E. (2013). Proteins involved in electron transfer to Fe(III) and Mn(IV) oxides by Geobacter sulfurreducens and Geobacter uraniireducens. Microbiology 159, 515-535. https://doi.org/10.1099/mic.0.064089-0.
92. Arslan, E., Schulz, H., Zufferey, R., Kunzler, P., and Thony-Meyer, L. (1998). Overproduction of the Bradyrhizobium japonicum c-Type Cytochrome Subunits of the cbb3 Oxidase in *Escherichia coli*. BIOCHEMICAL AND BIOPHYSICAL RESEARCH COMMUNICATIONS 251, 4.
93. Koppel, D.E. (1972). Analysis of macromolecular polydispersity in intensity correlation spectroscopy: the method of cumulants. The Journal of Chemical Physics 57, 4814-4820.
94. Provencher, S.W. (1979). Inverse problems in polymer characterization: direct analysis of polydispersity with photon correlation spectroscopy. Die Makromolekulare Chemie: Macromolecular Chemistry and Physics 180, 201-209.
95. Jumper, J., Evans, R., Pritzel, A., Green, T., Figurnov, M., Ronneberger, O., Tunyasuvunakool, K., Bates, R., Žídek, A., Potapenko, A. et al. (2021). Highly accurate protein structure prediction with AlphaFold. Nature 596, 583-589. https://doi.org/10.1038/s41586-021-03819-2.
96. van Kempen, M., Kim, S.S., Tumescheit, C., Mirdita, M., Lee, J., Gilchrist, C.L.M., Soding, J., and Steinegger, M. (2024). Fast and accurate protein structure search with Foldseek. Nat Biotechnol 42, 243-246. https://doi.org/10.1038/s41587-023-01773-0.
97. Li, Z., Jaroszewski, L., Iyer, M., Sedova, M., and Godzik, A. (2020). FATCAT 2.0: towards a better understanding of the structural diversity of proteins. Nucleic Acids Res 48, W60-W64. https://doi.org/10.1093/nar/gkaa443.